International Telecommunication Union

ITU-R

Radiocommunication Sector of ITU

Report ITU-R P.2145-1

(06/2013)

Model parameters for an urban environment for the physical-statistical wideband LMSS model in Recommendation ITU-R P.681

P Series

Radiowave propagation

International Telecommunication Union

Foreword

The role of the Radiocommunication Sector is to ensure the rational, equitable, efficient and economical use of the radio-frequency spectrum by all radiocommunication services, including satellite services, and carry out studies without limit of frequency range on the basis of which Recommendations are adopted.

The regulatory and policy functions of the Radiocommunication Sector are performed by World and Regional Radiocommunication Conferences and Radiocommunication Assemblies supported by Study Groups.

Policy on Intellectual Property Right (IPR)

ITU-R policy on IPR is described in the Common Patent Policy for ITU-T/ITU-R/ISO/IEC referenced in Annex 1 of Resolution ITU-R 1. Forms to be used for the submission of patent statements and licensing declarations by patent holders are available from http://www.itu.int/ITU-R/go/patents/en where the Guidelines for Implementation of the Common Patent Policy for ITU-T/ITU-R/ISO/IEC and the ITU-R patent information database can also be found.

Series of ITU-R Reports

(Also available online at http://www.itu.int/publications/R-REP/en)

Series	Title
BO	Satellite delivery
BR	Recording for production, archival and play-out; film for television
BS	Broadcasting service (sound)
BT	Broadcasting service (television)
F	Fixed service
M	Mobile, radiodetermination, amateur and related satellite services
P	**Radiowave propagation**
RA	Radio astronomy
RS	Remote sensing systems
SA	Space applications and meteorology
SF	Frequency sharing and coordination between fixed-satellite and fixed service systems
SM	Spectrum management

Note: *This ITU-R Report was approved in English by the Study Group under the procedure detailed in Resolution ITU-R 1.*

Electronic Publication
Geneva, 2014

REPORT ITU-R P.2145-1

Model parameters for an urban environment for the physical-statistical wideband LMSS model in Recommendation ITU-R P.681

(2009-2013)

Summary

This Report describes the physical-statistical wideband LMSS channel model in Recommendation ITU-R P.681 § 7, providing all background and relevant information.

Annex 1

CONTENTS

1 Introduction

The statistical data provided with the physical-statistical wideband land mobile satellite services (LMSS) channel model also named in this Report as the land mobile multipath channel model (LMSCM), was derived from measurement data recorded in a comprehensive high resolution channel sounding campaign in and around Munich in 2002. In this campaign different urban, suburban and rural environments were measured for car and pedestrian applications.

In these measurements the satellite of a potential navigation system was simulated by a Zeppelin NT. The Zeppelin transmitted the measurement signal between 1 460 and 1 560 MHz towards the ground using a hemispherical, circular polarized, antenna with 10W EIRP. The receiver was mounted in the measurement vehicle, which was driven through the measurement area. In the case of the pedestrian measurement the antenna was carried by the walking user followed by the measurement vehicle.

Based on this measurement data the LMSCM was developed. This model is a realistic high resolution deterministic-statistical model.

A receiver can be moved through a synthetic environment with houses, trees and lamp posts. These obstacles influence the LoS path. In addition reflectors are produced causing echo signals.

The statistical part of the model comprises:

– the house front, tree and lamp post generation in the synthetic environment;
– the position dependent LoS signal power variations in the shadow of tree tops;
– the position of reflectors dependent on the satellites azimuth and elevation;
– the mean power of echoes depending on their distance to the receiver and on the;
– satellite elevation;
– Rice factor and bandwidth of echo signals depending on the satellite elevation;
– the life span of echoes depending on the satellite elevation;

– the number of coexisting echoes in the channel depending on the satellite elevation;
– and the movement of reflection points, also depending on the satellite elevation.

Deterministically modelled are:

– the diffraction of the LoS signal on houses, tree trunks and lamp posts;
– the delay of diffracted signals received in the shadow of houses;
– the mean attenuation through tree tops;
– and the delay and Doppler shift trends of echo signals due to the receiver and reflector movement.

An important model feature is the high level of detail. Realistic correlation between echo signals is achieved due to the used reflector position statistics combined with the deterministically calculated delay and Doppler trends. Full satellite azimuth and elevation dependency is given for both LoS and the echo signals. As general model parameters the snapshot rate, the frequency band, the user type and the environment can be chosen.

Parameters for the distribution of e.g. house heights and widths, for tree and lamp post size and positions, but also for the street width and e.g. the receiver antenna height allow to model specific scenarios and to investigate their impact. High flexibility is also given by the way oriented deterministic and stochastic model approach. Receiver speed and heading input allows to simulate different movement situations, e.g. turns, a traffic jam, stop and go, or the relatively long stops at traffic lights. Also speeds which are even higher than during the measurement can be applied.

For a complete description of the measurement, the data analysis and the modelling of the satellite to earth multipath channel see also Lehner [2007].

The structure of this Annex is the following: Section 1 gives an introduction to the model, § 2 describes in detail the characteristics of the channel model and implementation features. Section 3 provide all features of the model which are dependent on the urban scenario where measurements were originally taken for the development of the model. Section 4 includes an Interface Control Document for users interested on understanding the software implementation or re-implement the model. Acronyms are found in § 6. Section 7 provides information on intellectual property rights associated to the models and References.

2 Software model download

The MATLAB implementation of the model needs only 140 KB disk space including the statistic data for the urban city center environment for car applications. It is a stand alone model generating its own scenery. The execution speed is reasonably fast with 250 complex channel impulse responses per second on a 1.5 GHz CPU. The model output is a complex time-variant channel impulse response with up to 80 discrete rays. Due to this time variant tapped delay line structure it can be easily incorporated in any simulator.

The complete model implemented in MATLAB can be downloaded from: http://www.kn-s.dlr.de/satnav/.

3 Physical-statistical wideband model for mixed propagation conditions

For broadband LMSS with a multipath propagation channel where different frequencies within the signal bandwidth are affected differently by the channel (frequency-selective channels), a model that implements a linear transversal filter whose output is a sum of delayed, attenuated and Doppler shifted versions of the input signal (wideband model) is more suitable. Definitions on multipath propagation are found in Recommendation ITU-R P.1407-2.

The model is given for a situation where a satellite is transmitting from a known position to a receiver on ground, where an elevation ε and an azimuth φ can be computed relative to the receiver heading and position. The model can be applied for frequencies between 1 and 2 GHz. It is suitable to serve the requirements of wideband transmission systems with a bandwidth up to 100 MHz. The model is based on deterministic and stochastic parameters and it is able to generate vectors that include complex envelope time-series of direct signal and reflections, with corresponding path delay vectors. The parameters determining the stochastic behaviour of the model are derived from measurements obtained on a given scenario.

The geometry of the model is based on a synthetic environment representation. In the scenery there is a local Cartesian coordinate system. To keep the model simple, the receiver is moving in the x-direction only. Turns (changes of the receiver heading) are modelled by changing the satellite azimuth. Therefore, the model azimuth is calculated by:

$$\varphi = \varphi_{Rx} - \varphi_{sat} \tag{1}$$

where:

φ_{Rx}: absolute heading of the receiver

φ_{sat} : absolute satellite azimuth.

For the movement model, in the local coordinate system the receiver position is calculated by:

$$x(t) = \int_0^t v_{Rx}(t)\,\mathrm{d}t \tag{2}$$

where $v_{Rx}(t)$ is the velocity of the receiver. The y and z coordinates stay constant during the simulation run.

The channel model is realized in a modular way consisting of a combination of the following parts:

– Shadowing of the direct signal:
  – house front module;
  – tree module;
  – light pole module;
– Reflections module.

The structure of the model is illustrated in Fig. 1 including the following input, intermediate and output time-variant signals:

$v_u(t)$: user speed
$hd_u(t)$: user heading
$el_s(t)$: satellite elevation
$az_s(t)$: satellite azimuth
$x_u(t)$: user position in x-axis (y and z axis are considered constant)
$az_u(t)$: user azimuth
$y_u(t)$: output signals, where each *i* is related to direct signal and reflectors.

FIGURE 1

Structure of the model

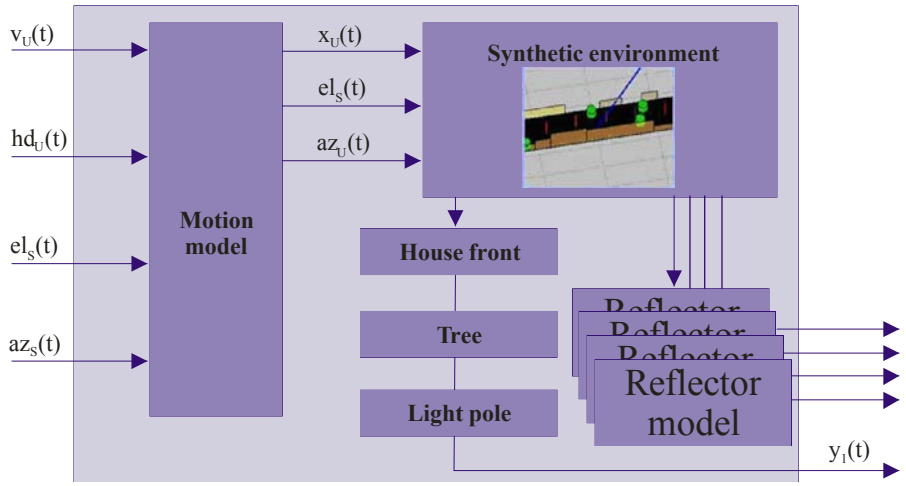

Report P.2145-01

3.1 Shadowing of the direct signal

The shadowing and diffraction of the direct signal path at house fronts, trees and light poles within the scenery is calculated from a single knife-edge model (see Recommendation ITU-R P.526). A sketch of the general geometry is given in Fig. 2.

FIGURE 2

Communicating antennas over an obstacle

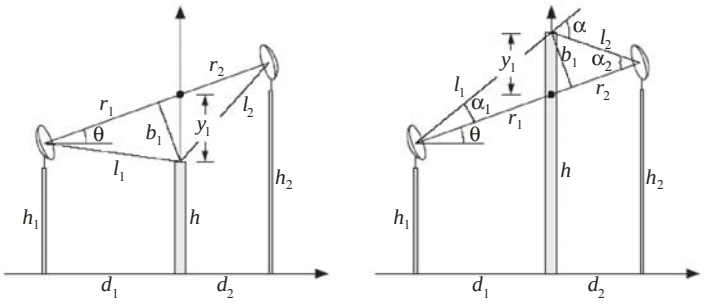

Report P.2145-02

With the normalized Fresnel variable:

$$\nu = b_1\sqrt{\frac{2}{\lambda}\frac{d_1+d_2}{d_1 d_2}} = y_1\cos(\theta)\sqrt{\frac{2}{\lambda}\frac{d_1+d_2}{d_1 d_2}} \tag{3}$$

the diffraction coefficient $D(\nu)$ can be computed from the Fresnel integral $F(\nu)$ by:

$$D(\nu) = \frac{1}{1-j}\left(F(\nu)+\frac{1-j}{2}\right) = \frac{1}{1-j}\left(\int_0^{\nu} e^{-j\frac{\pi}{2}u^2}\,du + \frac{1-j}{2}\right) \tag{4}$$

The distance y_1 is defined positive if there is a direct sight between the antennas, whereas it is negative if the considered obstacle is shadowing the signal, i.e. $y_1 = \begin{cases} -|y_1| & \text{if LoS shadowed} \\ |y_1| & \text{otherwise} \end{cases}$

3.1.1 House-front module

Let P denote the point where the direct signal between satellite and receiver intersects with the considered house front. Then diffraction occurs at the roof of the house above or below that point, and at the closest walls to the left and to the right of it (see Fig. 3):

– If the intersection point P falls inside a house (the direct ray is shadowed), the LoS signal is shadowed. In this case the model returns three paths, with relative delays, $\Delta\tau_{roof}$, $\Delta\tau_{wall,left}$, $\Delta\tau_{wall,right}$ and complex amplitude factor . $D(\nu_{roof})$, $D(\nu_{wall,left})$, $D(\nu_{wall,right})$ respectively corresponding to the roof, the left wall and the right wall around P.

– If the intersection point P does not fall inside a house (the direct ray is not shadowed), the model returns a single path with amplitude factor $D(\nu)$ corresponding to the smallest y_1 and with $\Delta\tau$ equal to zero.

FIGURE 3

Diffraction at roofs and walls of house front

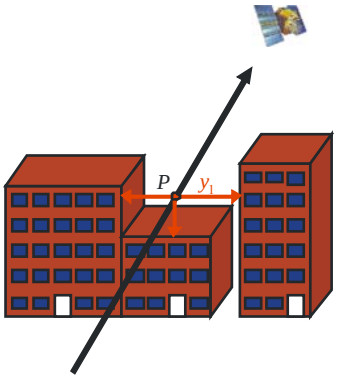

Report P.2145-03

The diffraction coefficients can be computed from the following variables:

Diffraction at house roof

The diffraction coefficient and relative delay due to diffraction at house roof are computed by the model according to the following steps:

Step 1: The distance between the intersection point P and the receiver on ground plane is calculated as follows:

$$d_1 = \sqrt{(x_P - x_{Rx})^2 + (y_P - y_{Rx})^2} \tag{5}$$

Step 2: The distance between P and the satellite is calculated as follows:

$$d_2 = \sqrt{(x_{Sat} - x_P)^2 + (y_{Sat} - y_P)^2} \tag{6}$$

Step 3: The distance between the vertical distance between *P* and house roof is calculated as follows:

$$\left|y_{1,roof}\right| = \left|X_P - X_{roof}\right| \tag{7}$$

Step 4: Calculate the normalized Fresnel variable ν_{roof} according to equation (3), θ being the elevation angle of the satellite from the receiver.

Step 5: The diffraction coefficient due to diffraction at house roof $D(\nu_{roof})$ is calculated according to equation (4).

Step 6: The path delay $\Delta\tau_{roof}$ is calculated as follows:

$$\Delta\tau_{roof} = \left(\sqrt{(z_{roof} - z_{Rx})^2 + d_1^2} - \frac{d_1}{\cos(\theta)} + y_1 \sin(\theta)\right) \cdot c_0 \tag{8}$$

Diffraction at house walls

The diffraction coefficients and relative delays due to diffraction at house walls are computed by the model according to the following steps:

Step 1: The distance between the intersection point *P* and the receiver on ground plane is calculated as follows:

$$d_1 = \sqrt{(x_P - x_{Rx})^2 + (y_P - y_{Rx})^2} \tag{9}$$

Step 2: The distance between *P* and the satellite is calculated as follows:

$$d_2 = \sqrt{(x_{Sat} - x_P)^2 + (y_{Sat} - y_P)^2} \tag{10}$$

Step 3: The vertical distances between *P* and the left and right house walls are calculated as follows:

$$\left|y_{1,left}\right| = \left|X_P - X_{wall,left}\right| \tag{11}$$

$$\left|y_{1,right}\right| = \left|X_P - X_{wall,right}\right| \tag{12}$$

Step 4: The angle θ is calculated as follows:

$$\arctan\left(\frac{\left|x_P - x_{Rx}\right|}{d_1}\right) \tag{13}$$

Step 5: The normalized Fresnel variables $\nu_{wall,left}$ and $\nu_{wall,right}$ are calculated according to equation (3), θ being the angle calculated at Step 4.

Step 6: The diffraction coefficients due to diffraction at house roof $D(\nu_{wall,left})$ and $D(\nu_{wall,right})$ are calculated according to equation (4).

Step 7: The path delays $\Delta\tau_{wall,left}$ and $\Delta\tau_{wall,right}$ are calculated as follows:

$$\Delta\tau_{wall,left} = \left(\sqrt{(z_{roof} - z_{Rx})^2 + d_1^2} - \frac{d_1}{\cos(\theta)} + y_{1,left} \sin(\theta)\right) \tag{14}$$

$$\Delta\tau_{wall,right} = \left(\sqrt{(z_{roof} - z_{Rx})^2 + d_1^2} - \frac{d_1}{\cos(\theta)} + y_{1,right} \sin(\theta) \right) \quad (15)$$

As mentioned in the introduction, if the intersection point *P* does not fall inside a house, the model returns a single path with amplitude factor $D(\nu)$ corresponding to min ($y_{1,roof}$, $y_{1,left}$, $y_{1,right}$) and with $\Delta\tau$ equal to zero.

3.1.2 Light pole module

Let *P* denote the point on the direct ray being closest to the axis of the light pole, and *d* be this closest distance (see Fig. 4). Consider the line through *P* that is orthogonal to the tree axis and to the direct ray. Diffraction occurs at the two points where this line intersects with the surface of the pole. The effect of these two sides of the pole is coherently added according to a double knife-edge diffraction model (see Recommendation ITU-R P.526):

$$D(\nu_{left}, \nu_{right}) = \frac{1}{1-j}\left(F(\nu_{left}) + \frac{1-j}{2} \right) + \frac{1}{1-j}\left(F(-\nu_{right}) + \frac{1-j}{2} \right) \quad (16)$$

Step 1: The distance from the point *P* to the pole axis is calculated as follows:

$$d = \sqrt{(x_{pole} - x_{Rx})^2 + (y_{pole} - y_{Rx})^2} \sin(\varphi_{sat} - \varphi_{pole}) \quad (17)$$

Step 2: The distance from the receiver to the point *P* is calculated as follows:

$$d_2 = \sqrt{({x_{Sat}}^2 - {x_P}^2) + ({y_{Sat}}^2 - {y_P}^2) + ({z_{Sat}}^2 - {z_P}^2)} \quad (18)$$

Step 3: The distance from the point *P* to the satellite is calculated as follows:

$$d_1 = \sqrt{(x_{pole} - x_{Rx})^2 + (y_{pole} - y_{Rx})^2} \frac{\cos(\varphi_{sat} - \varphi_{pole})}{\cos(\varepsilon_{sat})} \quad (19)$$

Step 4: The distance from the point *P* to the left and right intersection points with the surface of the pole are respectively calculated as follows:

$$b_{1,left} = y_{1,left} = d - R_{pole} \quad (20)$$

$$b_{1,right} = y_{1,right} = d + R_{pole} \quad (21)$$

Step 5: The normalized Fresnel variables ν_{left} and ν_{right} are calculated according to equation (3).

Step 6: The diffraction coefficient due to diffraction at light pole $D(\nu_{left}, \nu_{right})$ is calculated according to equation (4).

FIGURE 4

Diffraction at a light pole

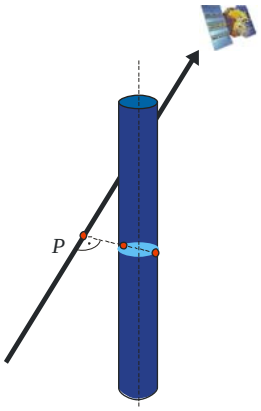

Report P. 2145-04

3.1.3 Tree module

Diffraction at the tree trunk

For the trunk of a tree the same double knife-edge model as for the light poles is considered in § 3.1.2.

Attenuation at the tree top

The attenuation factor caused by the top of a tree:

$$A_{tree}(x) = A_{cyl}(x) \cdot A_{stoch}(x) \tag{22}$$

is divided into a deterministic and a stochastic part (see Fig. 5). The deterministic term A_{cyl} is proportional to the length of the part of the direct ray that intersects with the cylinder of the tree model. It depends on the tree geometry and the specific attenuation γ_{tree} (see § 3.3).

The stochastic part is modelled by a Ricean fading process with the Gaussian way-power spectrum:

$$A_{stoch}(x) = \frac{1}{\sqrt{K_{tr}+1}}\left(\sqrt{K_{tr}}e^{j\varphi_c} + F^{-1}\left\{\sqrt{S_{tr}(X)}\right\}\right) \tag{23}$$

with

$$S_{tr}(X) = \frac{1}{\sqrt{2\pi\sigma^2}}\mathrm{e}^{-\frac{X^2}{2\sigma^2}} \tag{24}$$

and

$$\sigma = \frac{B_{tr}}{2\sqrt{2\ln(2)}}$$

where:

K_{tr} and B_{tr}: respectively denote the Rice factor and the 3-dB bandwidth of the spectrum (see § 3.3)

φ_c: phase which is chosen randomly between 0 and 2π for each tree according to a uniform distribution.

FIGURE 5

Diffraction and attenuation by a tree

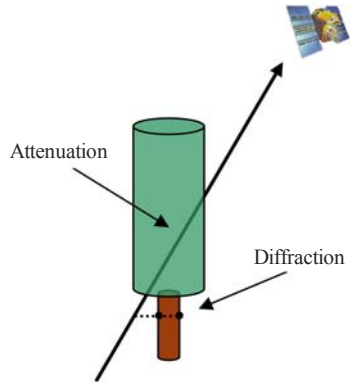

3.2 Reflections

The model uses reflectors that are realized as infinitively small spheres with a given attenuation to the direct path radiating equally in any direction. Based on these reflectors, a set of echoes is generated from a geometric position in the synthetic environment. The following sections deal with the generation of the echoes in terms of:

– position;
– lifespan;
– mean power (average and variation);
– fading (process, bandwidth, rice factor);
– reflector movement;
– number of echoes generation.

3.2.1 Synthesis of a single reflection

The likelihood of receiving an echo from a given reflector position is strongly dependent of the position of the reflector relative to the receiver and the satellite.

Horizontal position

The likelihood density distribution $P_{r,\psi}(\varepsilon, \varphi)$ for the existence of a reflector being present at a given position (polar coordinates r, ψ) is calculated as:

$$p_{r,\psi}(\varepsilon,\varphi) = \frac{p_{r,\psi}(\varepsilon) \cdot p_{\alpha-\varphi}(\varepsilon)}{\iint p_{r,\psi}(\varepsilon) \cdot p_{\alpha-\varphi}(\varepsilon) \mathrm{d}r\mathrm{d}\psi} \tag{25}$$

where ε is the satellite elevation; φ is the satellite azimuth; α is the right-hand oriented angle between the reflector and satellite seen from the receiver (see Fig. 6); $p_{r,\psi}(\varepsilon)$ is the probability density of a reflector being present at the horizontal position r, ψ, assuming an equal distribution of φ; and $p_{\alpha-\varphi}(\varepsilon)$ is the probability density of a reflector being present at the relative direction between φ and α (see § 3.3).

FIGURE 6

Relative angle, α

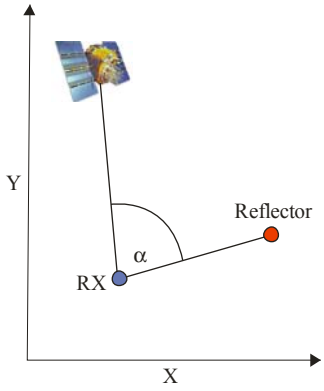

Report P.2145-06

Z-Position

To determine the Z-position of the reflector, assume that the elevation of the reflection ray does not change, since most of the reflecting walls are vertical.

Therefore, the reflector z coordinate is given by:

$$z = \min\left(\frac{r}{\cos(\varepsilon)}, h_b - h_{RX}\right) \tag{26}$$

where r is the distance between receiver and reflector, h_b is the height of a randomly-chosen building according to the building height distribution in the modelled environment, and h_{RX} is the antenna height above ground.

Echo power

The power radiated from a reflector is modelled by a Gaussian distribution:

$$p_e(P) = \frac{1}{\sqrt{2\pi}\sigma(r,\psi,\varepsilon)} \exp\left(-\frac{(P-\mu(r,\psi,\varepsilon))^2}{2\sigma(r,\psi,\varepsilon)^2}\right) \tag{27}$$

where $\sigma(r, \psi, \varepsilon)$ and $\mu(r, \psi, \varepsilon)$ are, respectively, the power variance and the power mean at the relative position (r, ψ) for the satellite elevation, ε (see § 3.3).

Echo fading

The isolated echo signal is modelled as a Rican fading process. This process is modelled by:

$$s_{stoch}(t) = \sqrt{P_e}\frac{1}{\sqrt{K}+1}\left(\sqrt{K}\exp(j\varphi_C) + F^{-1}\left\{\sqrt{S(f)}\right\}\right) \tag{28}$$

where:

p_e: selected echo power as in equation (27)

K: Rice factor (see § 3.3)

φ_C: randomly-chosen (uniformly distributed between 0 and 2π) initial phase of the constant part

$F^{-1}\{S(f)\}$: statistical process that in average fits to the spectrum $S(f)$, assumed to be Gaussian distributed:

$$S(f) = \frac{1}{\sqrt{2\pi\sigma}} \exp\left(-\frac{f^2}{2\sigma^2}\right) \tag{29}$$

where σ is given by:

$$\sigma = \frac{B_e}{2\sqrt{2\ln(2)}} \tag{30}$$

with B_e being the 3-dB bandwidth of the echo selected from the Gaussian probability density function $p_{be}(\varepsilon)$ (see § 3.3). The mean and variance of this bandwidth are derived from measurements for a given scenario.

The echo fading process is highly correlated with the movement of the receiver. Therefore, the complex value of the echo is modelled by:

$$s(x,t) = s_{stoch}(t) \cdot \exp\left(-j(\varphi_D(x) + \varphi_{i,R})\right) \tag{31}$$

where x is the x-position of the receiver, $\varphi_{i,R}$ is the randomly-chosen (uniformly distributed between 0 and 2π) initial phase of the echo, and φ_D is the deterministic Doppler phase shift due to the receiver movement given by:

$$\varphi_D(x) = \frac{|\vec{r}_r(x)|}{2\pi\lambda} \tag{32}$$

with $\vec{r}_r(x)$ the vector from the receiver to the reflection point, and λ, the wavelength.

The relative delay (with respect to the direct signal) of the echo can be calculated by:

$$\Delta\tau(x) = \frac{|\vec{r}_r(x)| - \vec{r}_r(x) \cdot \vec{r}_s(x)}{c_0} \tag{33}$$

where $\vec{r}_s(x)$ is the normalized vector from the receiver to the satellite.

Reflector life span

The echoes appear and disappear rapidly and often, their lifetime is highly dependent on the receiver speed. The lifespan is modelled as a function dependent on the travelled direction.

The actual life span is selected from a given cumulative distribution function, $P_{ls}(\varepsilon)$, derived from measurements for a given scenario (see § 3.3).

Reflector movement

Some reflection points tend to move parallel to the receiver movement; the rest of the points are assumed to be static. The probability of a reflector moving depends on the satellite elevation. This probability $\Pr\left(\text{mov}_{refl} \xleftrightarrow[\text{parallel}]{} \text{mov}_{Rx} \,/\, \varepsilon\right)$ is derived from measurements for a given scenario (see § 3.3).

3.2.2 Number of coexisting reflections

The number of coexisting echoes is modelled as a combination of a synthetically-generated wideband and narrow-band process, overlaid by a constant:

$$N(x,\varepsilon) = N_n(x,\varepsilon) + N_w(x,\varepsilon) + \overline{N}(\varepsilon) \tag{34}$$

where:

$N_n(x,\varepsilon)$: narrow-band process (with a Gaussian distributed amplitude)

$N_w(x,\varepsilon)$: wide band process (also with a Gaussian distributed amplitude)

$\overline{N}(\varepsilon)$: constant describing the average number of echoes.

The power spectral density of the process $PSD\{N(x,\varepsilon)\}$, and the mean value $\overline{N}(\varepsilon)$, are derived from measurements for a given scenario (see § 3.3).

3.3 Model parameters for an urban environment

Table 1 summarizes the inputs to the different elements of the model that are scenario-dependent and derived from data. For the use of the model as a whole, synthetic scenery needs to be generated with given characteristics for the size and distribution of trees, light poles and buildings in the scenery. In § 4 the parameters for the generation of this scenery for the measured case in Munich are included.

TABLE 1

Scenario-dependant parameters and functions extracted from data files

Parameter	Description
γ_{tree}	Specific attenuation (dB/m) for the deterministic part of tree attenuation A_{cyl}
K_{tr}	Rice factor tree attenuation Ricean fading process A_{stoch}
B_{tr}	3-dB bandwidth of tree attenuation Ricean fading process A_{stoch}
$p_{r,\psi}(\varepsilon)$	Probability density of a reflector being present at the horizontal position, r, ψ, assuming an equal distribution of the satellite azimuth φ
$p_{\alpha\text{-}\varphi}(\varepsilon)$	Probability density of a reflector being present at the relative direction between the azimuth φ and the angle α between reflector and satellite seen from the receiver
$\mu(r, \psi, \varepsilon)$	Power mean at the relative position (r, ψ) observed in the measurement for the satellite elevation ε
$\sigma(r, \psi, \varepsilon)$	Power variance at the relative position (r, ψ) observed in the measurement for the satellite elevation ε
B_e	3-dB bandwidth of the echo selected from the Gaussian probability density function $p_{be}(\varepsilon)$ with mean and variance depending on elevation ε

K	Rice factor of the echo fading Ricean process
$P_{ls}(\varepsilon)$	Cumulative distribution function of the life span of a reflector as a function of elevation ε
$Pr\left(\text{mov}_{refl} \xleftrightarrow[\text{parallel}]{} \text{mov}_{Rx} / \varepsilon\right)$	Probability that a reflector moves parallel to the receiver, depending on elevation ε
$\overline{N}(\varepsilon)$	Constant describing the average number of echoes as a function of elevation ε
$PSD\{N(x,\varepsilon)\}$	Power spectral density of the process (narrow-band plus wideband) describing the number of echoes as a function of elevation ε

3.4 Model input

For every input sample some values must be given for the model input:

– satellite elevation

– satellite azimuth

– user speed

– user heading.

Please note that the user speed is limited by the sampling frequency:

$$v < \frac{c_0 \cdot f_{samp}}{f_c \cdot 2} \tag{35}$$

Where f_{samp} is the sampling frequency, f_c is the carrier frequency and c_0 is the speed of light. It is recommended to use some over-sampling factor.

3.5 Model output

The model outputs a vector of N path delays τ_i and N complex values $A_i(t)$ for every time instance. The equivalent baseband channel impulse response is given by:

$$h(t,\tau) = \sum_{i=1}^{N} A_i(t) \cdot \delta(\tau - \tau_i(t)) \tag{36}$$

where t and τ indicate time and delay axes respectively. Please note that the path delays $\tau_i(t)$ are time-variant and they can reach arbitrary values.

The following figures give an example of the model output. For these figures the user speed was set to $v(t) = (\sin(t + t_0) + 1) \cdot v_{max}$. In Fig. 7 the red dashed line shows the maximum possible Doppler frequency according to the current user speed and the carrier frequency. The other coloured lines show the Doppler frequency of the echoes – their width is proportional to the actual power. At instances t = 4,7 s the car came to a full stop which reduces the Doppler to a minimum driven by the time driven fading process.

Figure 8 shows the Delay variation of the reflections. Due to the given life span, the life time of the reflections is dependent of speed. In regions where the receiver speed is high the echo life time is short but in regions with low user speeds the echoes can live for a long time.

FIGURE 7

Model output – Echo Doppler

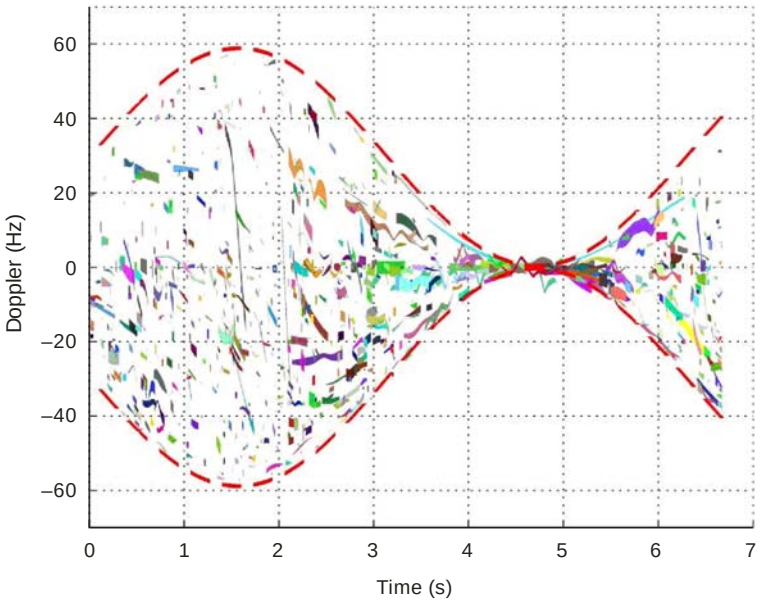

Report P.2145-07

FIGURE 8

Model output – Echo delay

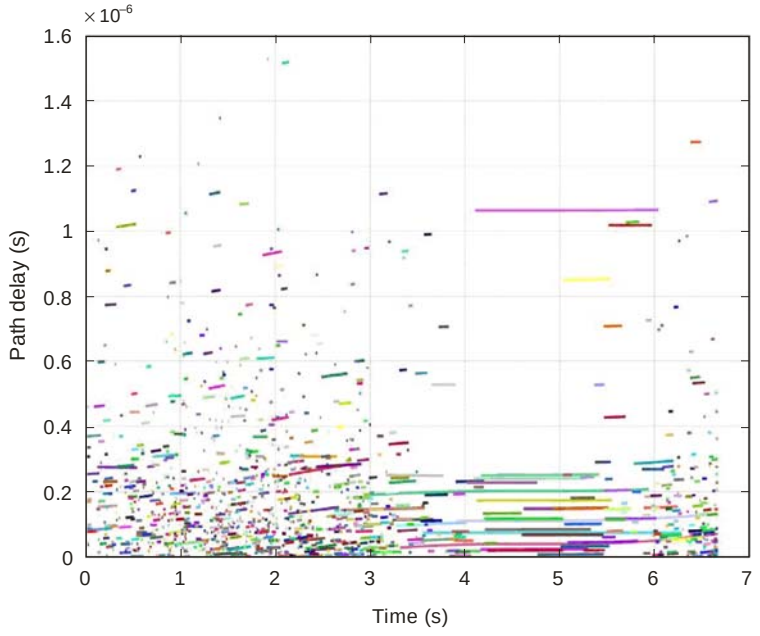

Report P.2145-08

3.6 Model output usage

Let $s(t)$ be the transmitted equivalent baseband signal, then the received signal $r(t)$ can be calculated in the usual way, by the convolution of the transmitted signal with the channel impulse response as:

$$r(t) = s(t) * h(t, \tau) \tag{37}$$

The channel impulse responses as model output are updated at a rate given by f_{samp}.

The delay axis τ of the output is continuous, thus, in order to implement the channel impulse response into a FIR filter a discretization of the delay axis is required. This is done by interpolation as explained in § 3.7.

3.7 User Implementation Features: interpolation of series of time-continuous discrete impulses to FIR filter coefficients

The time-continuous CIR time series provided by channel models have to be converted to the discrete-time sampling grid to be applicable in simulation software. Several options for this interpolation process are possible.

Two different types of interpolation methods are lined out within this document. The first procedure is the standard time domain low-pass interpolation method using a $\sin(x)/x$ formulation. It is shown that the usage of this method results in a fluctuating and unsatisfying phase response in the case of time-continuous echoes as inputs.

The introduced frequency domain method demonstrates far better results from a phase response point of view.

To clarify the process, examples with three Dirac impulses (which could represent a CIR) are calculated in the next sections.

To provide a sanity check of the described procedure, in § 3.7.1 first assumes that the given echo impulses sit directly on sampling instants. Secondly, § 3.7.2 describes the time domain low-pass interpolation and § 3.7.3 introduces the frequency domain method.

All these sections carry out the example calculation with a sampling frequency of $f_{smpl} = 25$ MHz whereas § 3.7.4 gives a comparison of the interpolation methods' properties for the same example but at sampling frequency of 100 MHz.

3.7.1 Low-pass interpolation of sampling points matching Dirac input impulses

For the following example calculation, a sampling frequency of $f_{smpl} = 25$ MHz is assumed. Three Dirac-like impulses are given which lay exactly on sampling instants:

$$\begin{aligned} T_n(0) &= 0\text{s} \\ T_n(1) &= 0.12 \times 10^{-6}\text{s} \\ T_n(2) &= 0.36 \times 10^{-6}\text{s} \end{aligned} \tag{38}$$

and they possess the following complex weights:

$$A_n(0) = 1$$

$$A_n(1) = 0.87 \cdot \mathrm{e}^{j\left(\frac{1}{4}\pi\right)} \tag{39}$$

$$A_n(2) = 0.24 \cdot \mathrm{e}^{j(-0.37 \cdot \pi)}$$

The complete input signal can be written as:

$$x(t) = \sum_{k=0}^{m} A_n(k) \cdot \delta(t - T_n(k)) \tag{40}$$

Here, the considered time duration shall span from $t = 0$ s until $t = 0.44 \times 10^{-7}$ s. Figure 9 shows a plot of $x(t)$'s magnitude.

$x(t)$ can now be interpolated at the sampling points:

$$t_n = n \cdot \frac{1}{f_{smpl}}, \quad n = 0,1,...,11 \tag{41}$$

using the low-pass interpolation formula [Kammeyer and Kroschel, 2002]:

$$h(t_n) = \sum_{k=0}^{m} A_n(k) \cdot si[\omega_{max}(t - T_n(k))] \tag{42}$$

where:

$$si(x) = \frac{\sin(x)}{x} \tag{43}$$

and

$$\omega_{max} = 2\pi \frac{f_{smpl}}{2} \tag{44}$$

The magnitude plot of the resulting 12 interpolated points can be seen as red crosses in Fig. 10. The continuous lines show the values of the single si-function for every Dirac impulse. The black line shows the resulting sum of the three functions.

The two subsequent sections examine the case when the Dirac impulses occur on time instants which do not match sampling points.

FIGURE 9

Example signal with three complex Dirac impulses at time instants that match sampling points. Magnitude plot

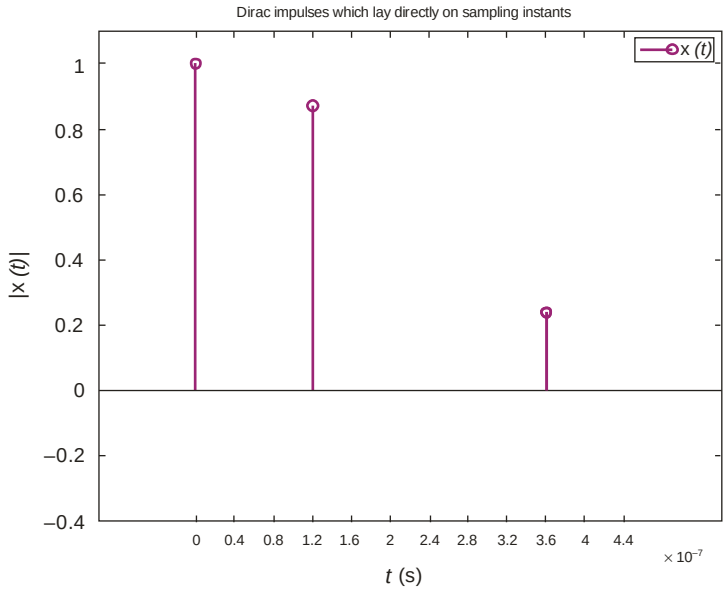

Report P. 2145-09

FIGURE 10

Interpolated with three complex Dirac impulses at time instants that match sampling points. Magnitude plot

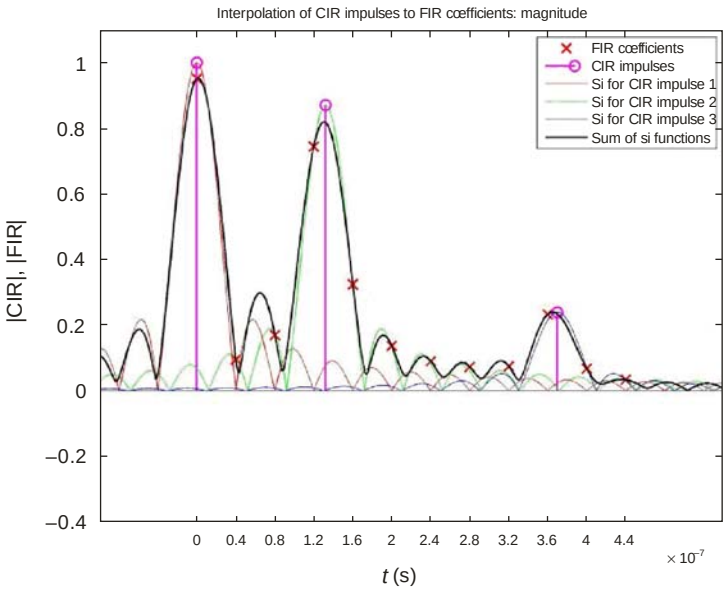

Report P. 2145-10

FIGURE 11

Interpolated $x(t)$ with three complex Dirac impulses at time instants that match sampling points. Phase plot

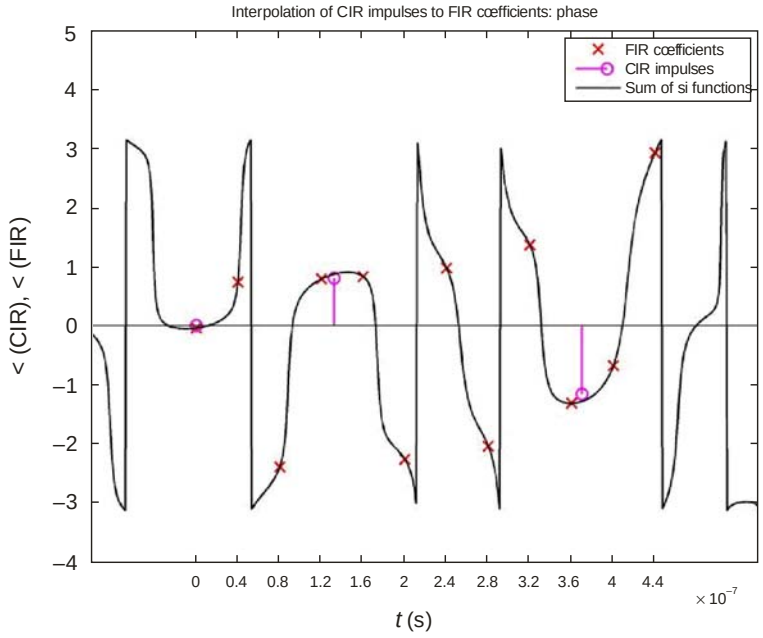

3.7.2 Low-pass interpolation of time-continuous Dirac input impulses

The same complex weights as given in equation (39) are used again, but compared to the times in equation (38) the last two impulses are slightly shifted to the following time instants:

$$T_n(0) = 0 \tag{45}$$

$$T_n(1) = 0.132 \times 10^{-6}\,\text{s} \tag{46}$$

$$T_n(2) = 0.37 \times 10^{-6}\,\text{s} \tag{47}$$

Figures 12 and 13 show the amplitude and phase plots of the interpolation. Since the impulses are not on sampling points anymore, the si-functions are shifted and the resulting sum of si-functions does not become 0 at the sampling instants. These residuals are called interpolation artefacts.

Every echo is represented by a $sin(x)/x$ function. The sum of all these functions is the interpolation result, as seen in the figure as a black curve. This result is sampled at the sampling instants given by the x-axis ticks and the corresponding red crosses. These values directly represent the FIR coefficients that can be used later in simulation program for the interpolation process.

FIGURE 12

Low-pass interpolation of the example echoes. The instants in time when the impulses occur do not match sampling instants. The LoS and the two echoes are illustrated as magenta Dirac-like stems with circles on top. A weighted *sin*(*x*)/*x* function represents every echo (green, red and blue curves). The resulting sum is given by the black line. The sampled FIR coefficients are represented by red crosses. This plot shows the data component's magnitude

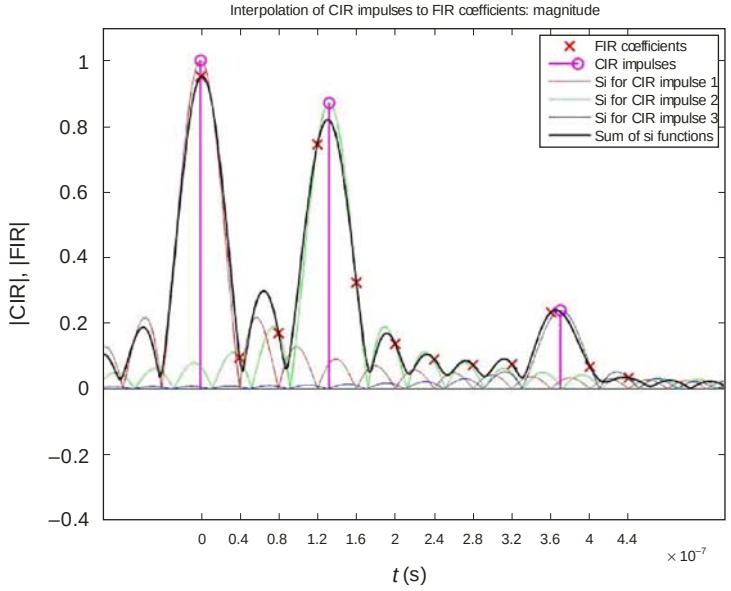

Report P.2145-12

FIGURE 13

Same as Fig. 12, but this plot shows the data component's phase

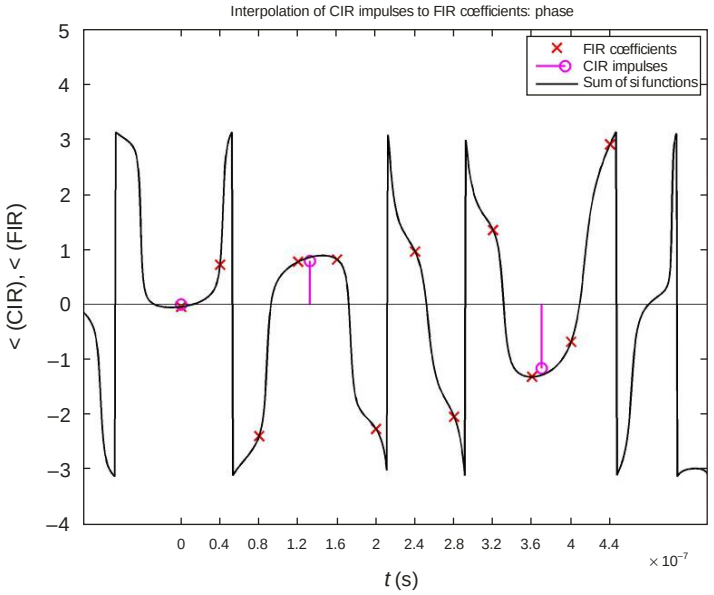

Report P.2145-13

3.7.3 Interpolation of time-continuous Dirac input impulses in frequency domain

Another interpolation method can be formulated using Fourier transform. Since the Fourier transform of the Dirac function $\delta(t)$ is given by:

$$\Im\{\delta(t)\}=1 \tag{48}$$

the Fourier transform's linearity is given by Sklar [1998]:

$$\Im\{A\cdot f(t)\}=A\cdot F(\omega) \tag{49}$$

and the Fourier transform's time-shift property states Sklar [1998]:

$$\Im\{f(t-\tau)\}=F(\omega)\mathrm{e}^{-j\omega\tau} \tag{50}$$

Where $\omega = 2\pi f$. An echo at time instant δ_0 with weight A can thus be transformed to frequency domain using:

$$\Im\{A\cdot\delta(t-\tau)\}=A\cdot\mathrm{e}^{-j\omega\tau} \tag{51}$$

A CIR consisting of multiple echoes can thus be calculated by a sum of such complex exponential functions:

$$\Im\left\{\sum_{n=0}^{N}A_n\cdot\delta(t-\tau_n)\right\}=\sum_{n=0}^{N}A_n\cdot\mathrm{e}^{-j\omega\cdot\tau_n} \tag{52}$$

Figures 14 and 15 show the magnitude and phase plot of this Fourier transform with the given sample echoes.

The subsequent step is to carry out the inverse Fourier transform of this frequency domain signal to obtain the interpolated points in time domain. The result of this computation using the inverse discrete Fourier transform (IDFT) is shown as magnitude plot in Fig. 16 and phase plot in Fig. 17.

The comparison of the low-pass interpolation result's phase plot (the red crosses in Fig. 13) and the frequency domain version (the red crosses in Fig. 17) shows a much smoother and realistic phase transitions for the interpolated FIR coefficients that originated by the frequency domain method. The phase jumps that occur from one red-crossed point to the other for the time domain version might severely affect a simulation program. In contrary, the frequency domain result provides a very linear phase characteristic in between the instance where the Dirac impulses occurred.

FIGURE 14

Interpolation in frequency domain: Sum of complex exponential functions and the resulting FIR coefficients. The magnitude is shown

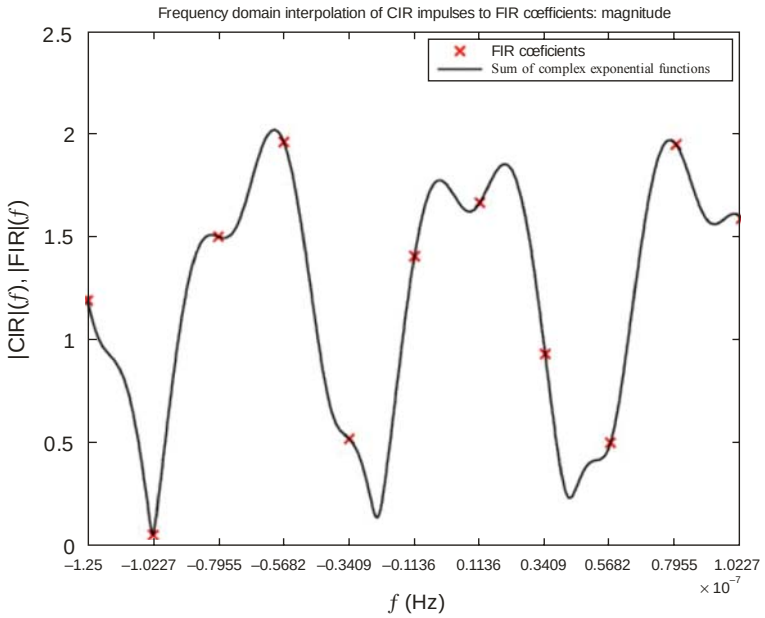

Report P.2145-14

FIGURE 15

Interpolation in frequency domain: Sum of complex exponential functions and the resulting FIR coefficients. The phase is shown

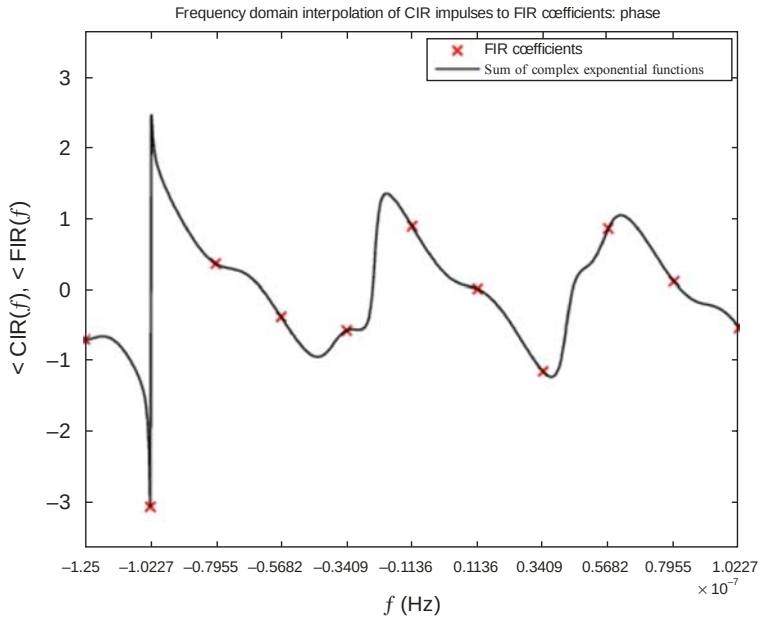

Report P.2145-15

FIGURE 16

The inverse Fourier transform of data given in Figs 14 and 15 leads to the wanted FIR coefficients in time domain. The coefficients' magnitude is plotted

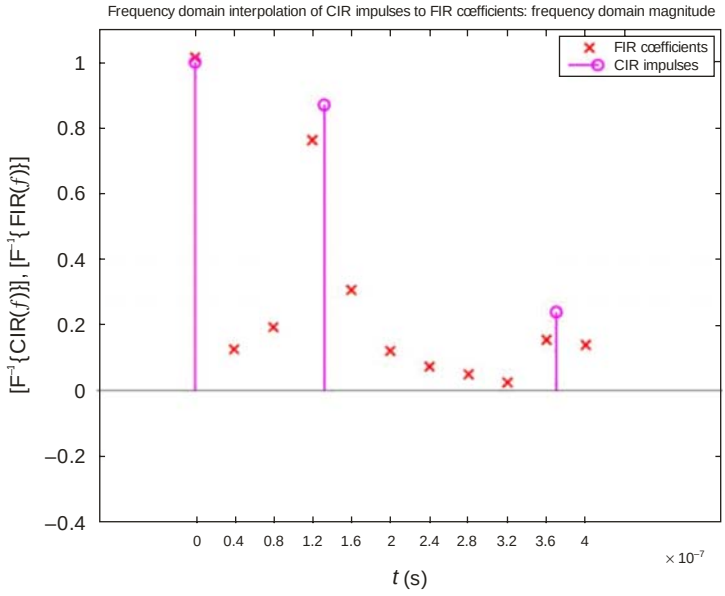

Report P.2145-16

FIGURE 17

The inverse Fourier transform of data given in Figs 14 and 15 leads to the wanted FIR coefficients in time domain. The coefficients' phase is plotted

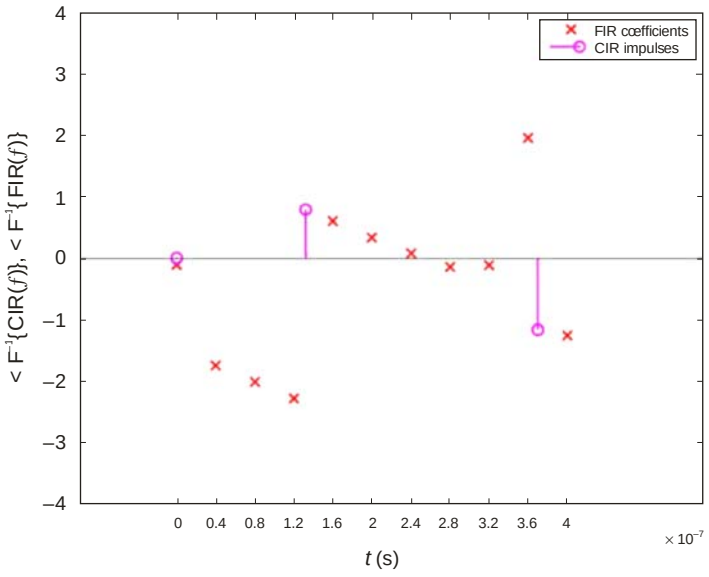

Report P.2145-17

3.7.4 Comparison of the interpolation methods with a sampling frequency of 100 MHz

All examples above where calculated using a sampling frequency of 25 MHz. The effect of the phase distortions which are caused by the low-pass interpolation becomes even more visible, when a higher sampling rate is chosen. The following four plots provide the direct comparison between low-pass and frequency domain interpolation of the example data at 100 MHz. Figures 18 and 19 show the magnitude and phase plot of the low-pass interpolation result and Figs 20 and 21 show the

result for the frequency domain method. Once again, the phase response of the frequency domain method is very linear whereas the low-pass interpolation generates high phase jumps which will cause negative influences on a simulation routine.

FIGURE 18

Low-pass interpolation of sample impulses at 100 MHz sampling frequency. Magnitude plot

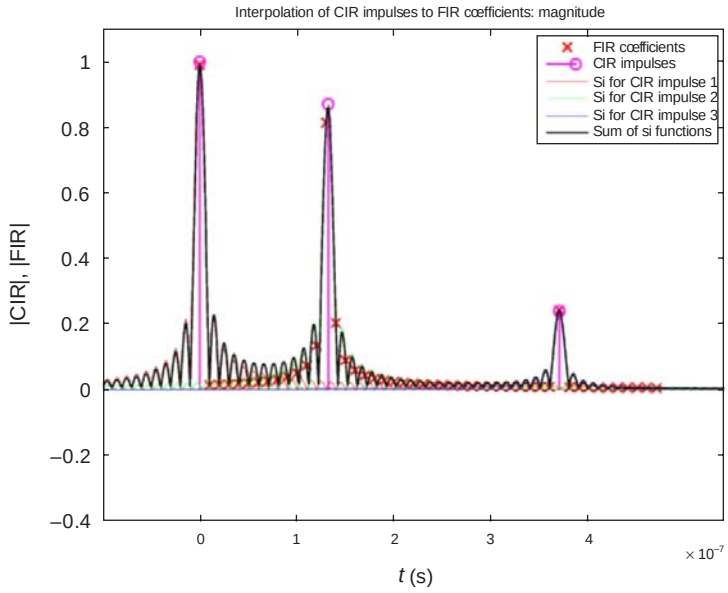

Report P.2145-18

FIGURE 19

Low-pass interpolation of sample impulses at 100 MHz sampling frequency. Phase plot

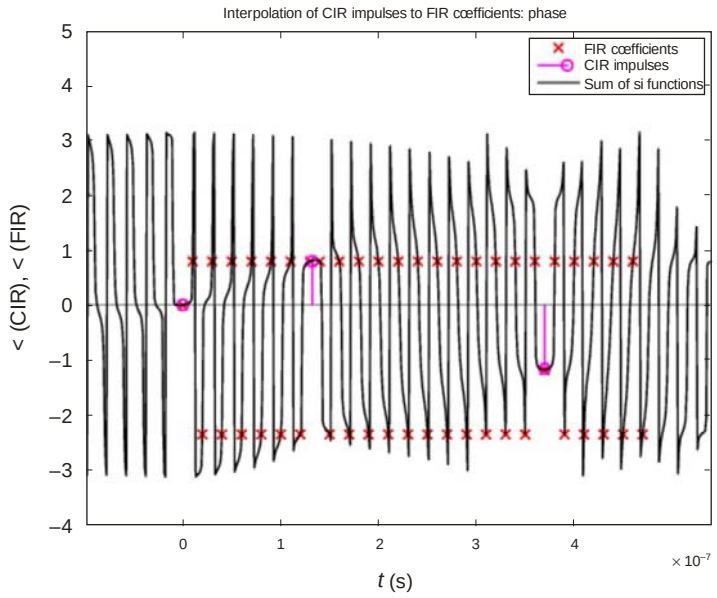

Report P.2145-19

FIGURE 20

Frequency domain interpolation of sample impulses at 100 MHz sampling frequency. Magnitude plot

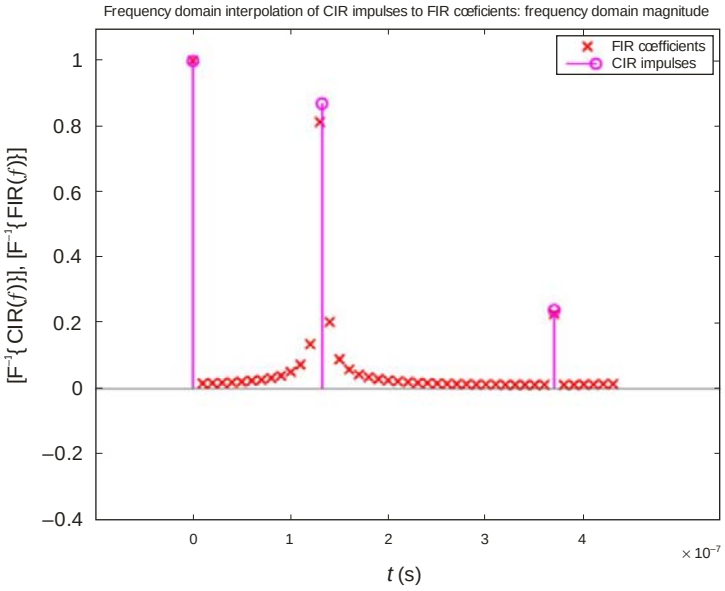

Report P. 2145-20

FIGURE 21

Frequency domain interpolation of sample impulses at 100 MHz sampling frequency. Phase plot

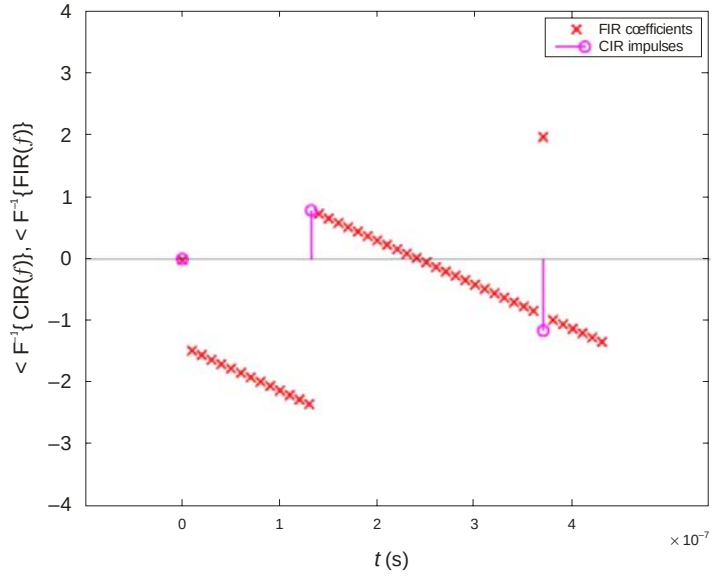

Report P. 2145-21

4 Report on physical-statistical wideband LMSS model in urban and suburban scenarios in Munich

In the next section, the measurements used to derive the model parameters are described. Data for the following environments are provided:

– Urban vehicle

– Suburban vehicle

– Urban pedestrian
– Suburban pedestrian

4.1 Environment description

4.1.1 Urban measurements

The measurements for the urban environment have been carried out in Munich (Germany). From the beginning of these measurements the satellite elevation has been seen as an important parameter for the measurement. Therefore the track of the measurement receiver has been selected in a way that it is highly concentrated around the centre spot of the measurement. This ensured that although the car was driving along its track the elevation is not changing very much during one measurement. Although this requirement was fulfilled the track has been selected to provide typical mixture of architecture for this environment.

FIGURE 22

Measurement Area "Urban" in Munich

Report P.2145-22

Figure 22 shows the car track in the "Lindwurmstrasse" area in Munich. This road is one of the main roads of the capital of the German federal state of Bavaria. The track was followed by narrow roads, street canyons and large squares. For this low elevation the visibility of the satellite is naturally quite low as well.

FIGURE 23

Measurement Area "Lindwurmstrasse" in Munich

Report P. 2145-23

Figure 23 shows a typical wide road in Munich. In these roads trees can often be found on the sides of the road. The buildings are typically around 6 floors high. The road has 4-6 lanes in total.

FIGURE 24

Measurement Area "Oberanger" in Munich

Report P. 2145-24

Figure 24 shows a typical narrow street in Munich. This scenario is the often feared "urban canyon". It has only 2-4 lanes in total but in contrast to the wide street scenario most of the sky is shadowed.

4.1.2 Suburban city

The suburban measurements have been performed in the small town of Fürstenfeldbruck near Munich (48°10'39.02"N, 11°15'22.12"E). Figure 25 gives an impression of the measurement area. In comparison to the city of Munich the buildings of Fürstenfeldbruck are significantly lower (usually only three floors) and the streets are wider (see Figs 26 and 27).

FIGURE 25

Measurement Area "Suburban" in Fürstenfeldbruck

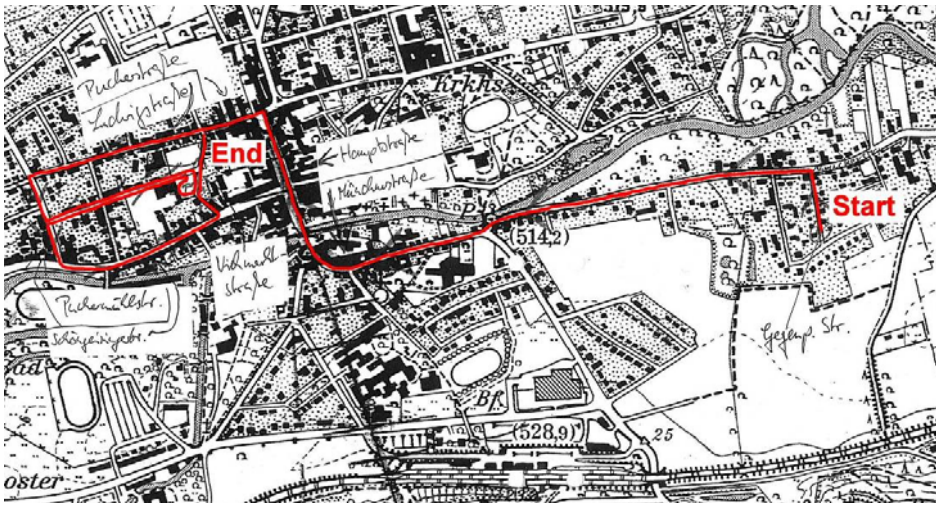

Report P.2145-25

FIGURE 26

City of Fürstenfeldbruck – Main street – View N to S

Report P.2145-26

FIGURE 27

City of Fürstenfeldbruck – Main street – View S to N

Report P.2145-27

4.2 Model description of scenario specific features

As described in the previous section, the model was developed from measurements in an urban scenario in both the old town and the modern part of Munich, Germany. Munich is one of the largest cities in Germany. The following scenarios are incorporated into the statistics:

– Wide streets, 30-50 m

– Narrow streets, 20-25 m

– City squares.

The model contains a set of parameters that can be configured to adapt the house fronts, trees and light poles in the environment. In § 4.3.2, a scenario is provided that matches the situation of the measured environment. The parameters can be tuned to other environments; however, those changes only affect the direct signal. For an accurate representation of the scenario, all scenario-dependent parameters in Table 2 would need to be estimated.

The data are included in data files available in the model software implementation. The File Interface Description for the files is given in § 5.

TABLE 2

Scenario-dependant parameters and functions extracted from data files

Parameter	Description	Value
γ_{tree}	Specific attenuation (dB/m) for the deterministic part of tree attenuation A_{cyl}	See § 4.3.3
K_{tr}	Rice factor tree attenuation Ricean fading process A_{stoch}	30
B_{tr}	3 dB bandwidth of tree attenuation Ricean fading process A_{stoch}	0.437 (1/m)

TABLE 2 (*end*)

Parameter	Description	Value
$p_{r,\psi}(\varepsilon)$	Probability density of a reflector being present at the horizontal position, r, ψ, assuming an equal distribution of the satellite azimuth φ	See Fig. 28
$p_{\alpha\text{-}\varphi}(\varepsilon)$	Probability density of a reflector being present at the relative direction between the azimuth φ and the angle α between reflector and satellite seen from the receiver	See Fig. 29
$\mu(r, \psi, \varepsilon)$	Power mean at the relative position (r, ψ) observed in the measurement for the satellite elevation ε	See Fig. 30
$\sigma(r, \psi, \varepsilon)$	Power variance at the relative position (r, ψ) observed in the measurement for the satellite elevation ε	See Fig. 31
B_e	3 dB bandwidth of the echo selected from the Gaussian probability density function $p_{be}(\varepsilon)$ with mean and variance depending on elevation ε	See Figs 32 and 33
K	Rice factor of the echo fading Ricean process	See Fig. 34
$P_{ls}(\varepsilon)$	Cumulative distribution function of the life span of a reflector as a function of elevation ε	See Fig. 35
$\Pr(\mathrm{mov}_{refl} \xleftrightarrow[\text{parallel}]{} \mathrm{mov}_{Rx} / \varepsilon)$	Probability that a reflector moves parallel to the receiver, depending on elevation ε	See Fig. 36
$\overline{N}(\varepsilon)$	Constant describing the average number of echoes as a function of elevation ε	See Fig. 37
$\mathrm{PSD}\{N(x,\varepsilon)\}$	Power spectral density of the process (narrow-band plus wideband) describing the number of echoes as a function of elevation ε	See Fig. 38

4.2.1 Urban vehicle

FIGURE 28

Probability density of a reflector being present at a horizontal position relative to the receiver

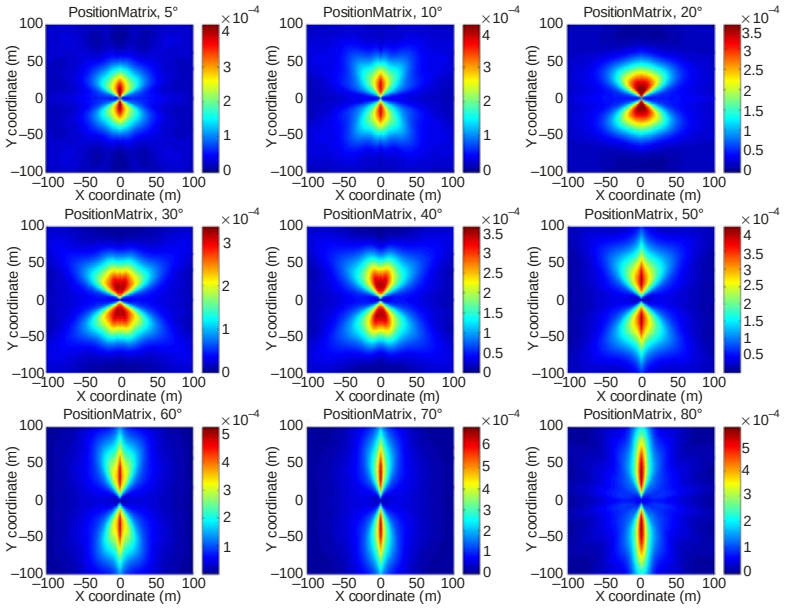

Report P. 2145-28

FIGURE 29

Likelihood of a reflector being present at a certain relative azimuth angle between reflector and LoS

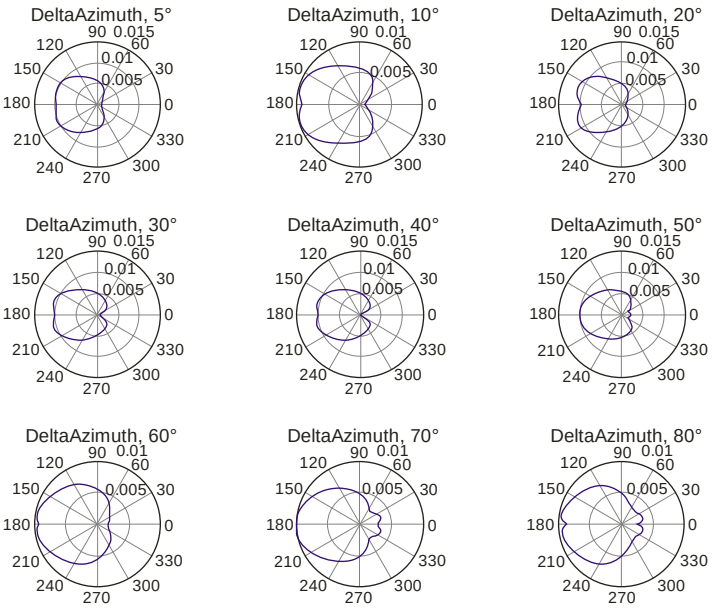

Report P. 2145-29

FIGURE 30

Mean power of a reflector for a certain horizontal position relative to the receiver

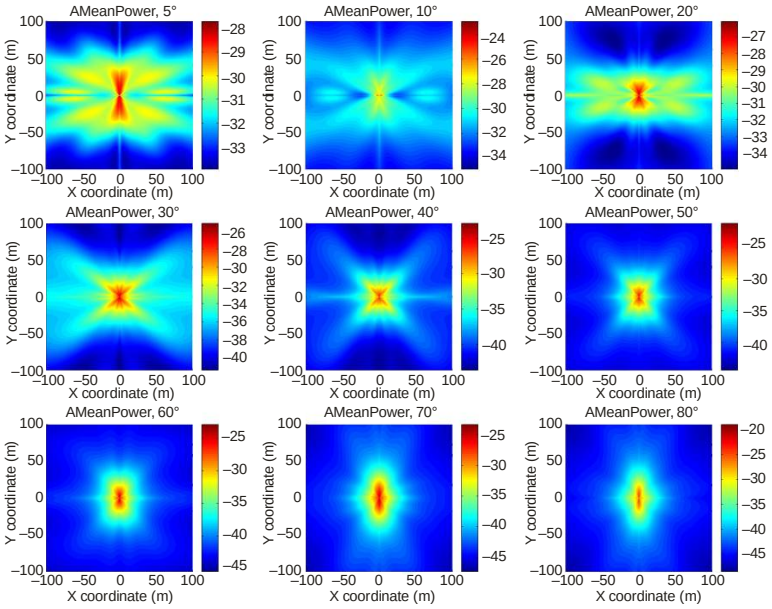

Report P. 2145-30

FIGURE 31

Standard deviation of the mean power of a reflector for a given relative horizontal position of a reflector

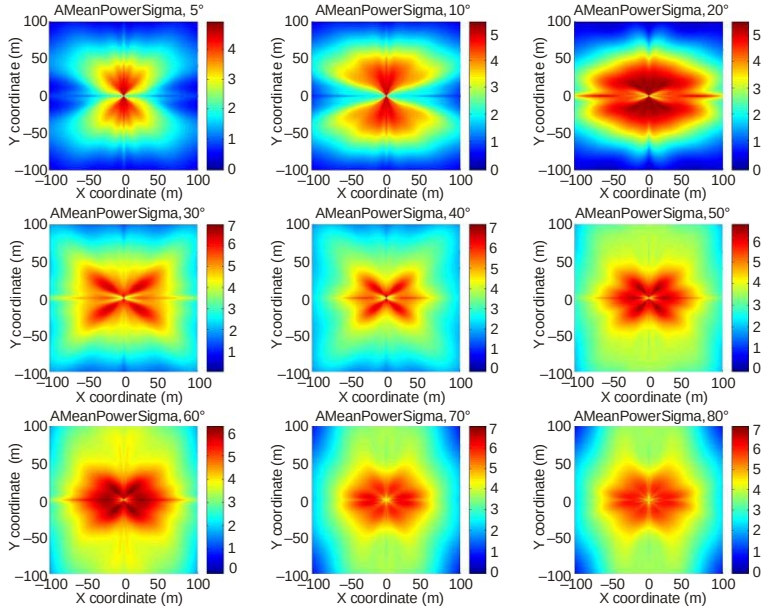

Report P. 2145-31

FIGURE 32

Mean value of the bandwidth of an echo as a function of the satellite elevation

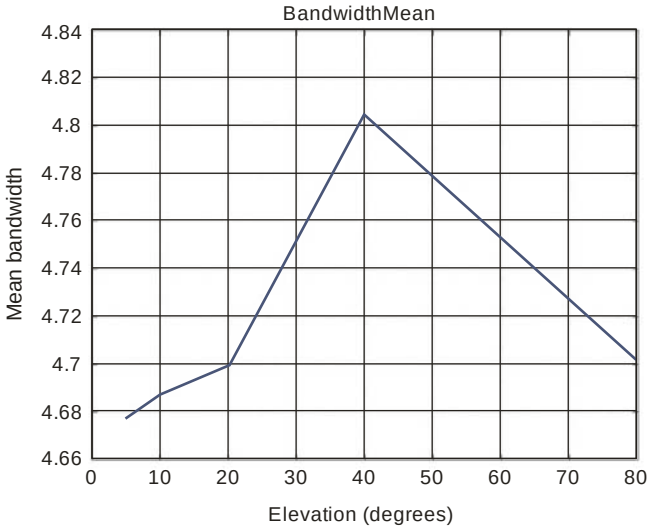

Report P. 2145-32

FIGURE 33

Standard deviation of the bandwidth of an echo as a function of the elevation angle

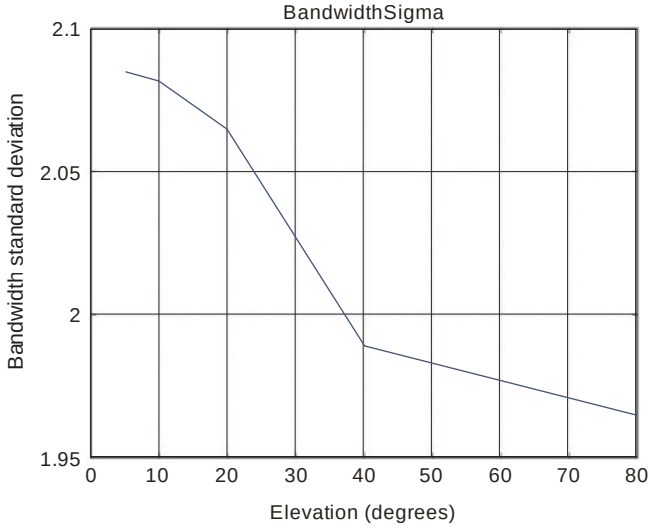

Report P. 2145-33

FIGURE 34

Cumulative distribution function of the Rice factors as a function of the elevation angle

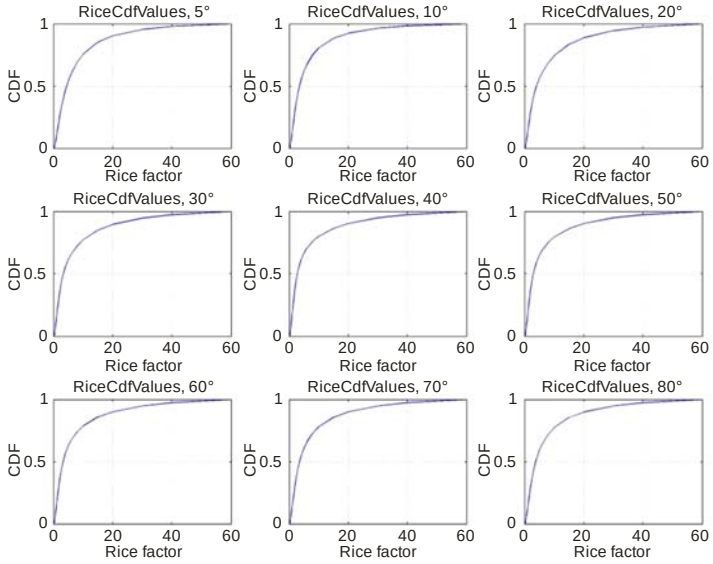

Report P.2145-34

FIGURE 35

Cumulative density function of the life span as a function of the elevation angle

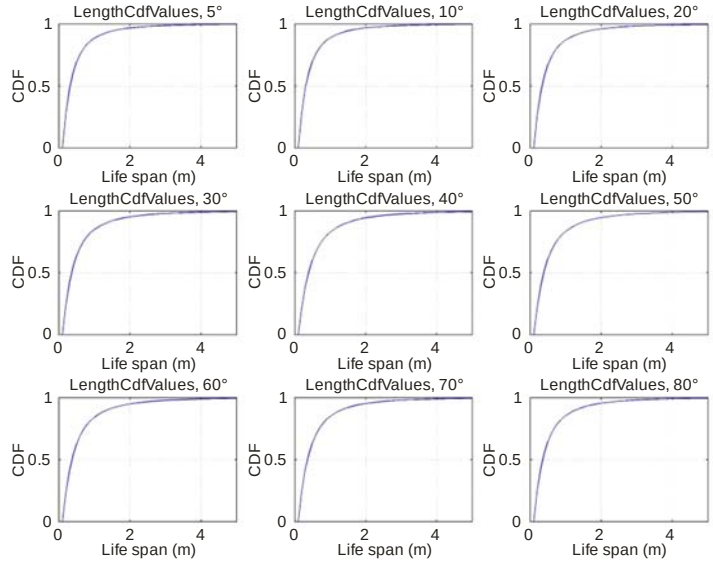

Report P.2145-35

FIGURE 36

Probability that a reflector is moving in the same direction as the receiver as a function of the elevation angle

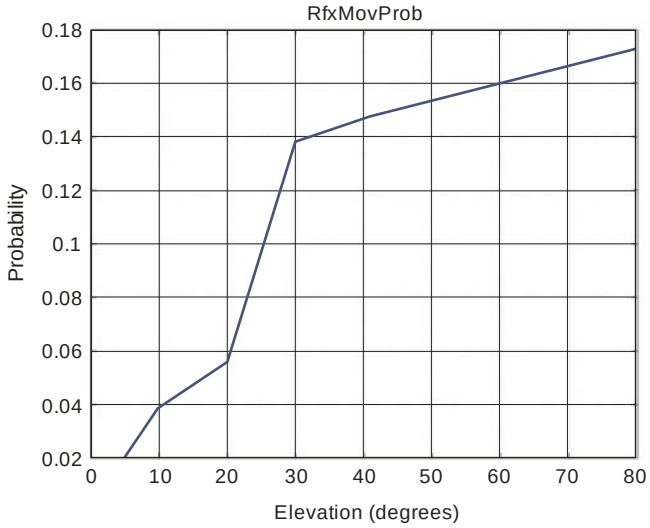

Report P.2145-36

FIGURE 37

Mean number of coexisting reflectors as a function of the elevation angle

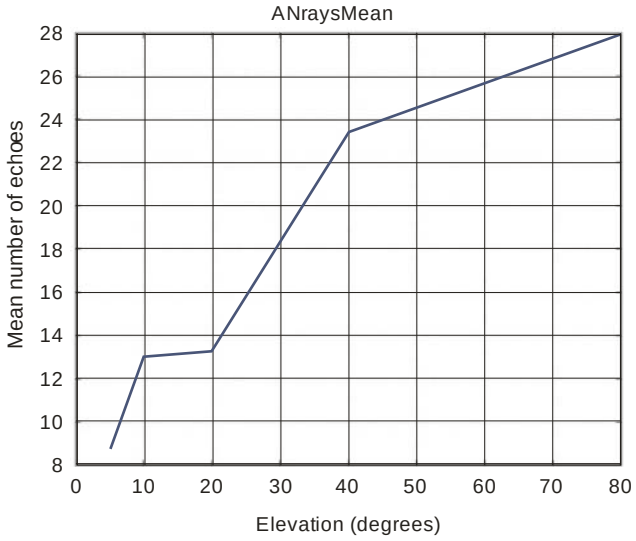

Report P.2145-37

FIGURE 38

Spectrum of the variation of the number of echoes over distance travelled in the x direction

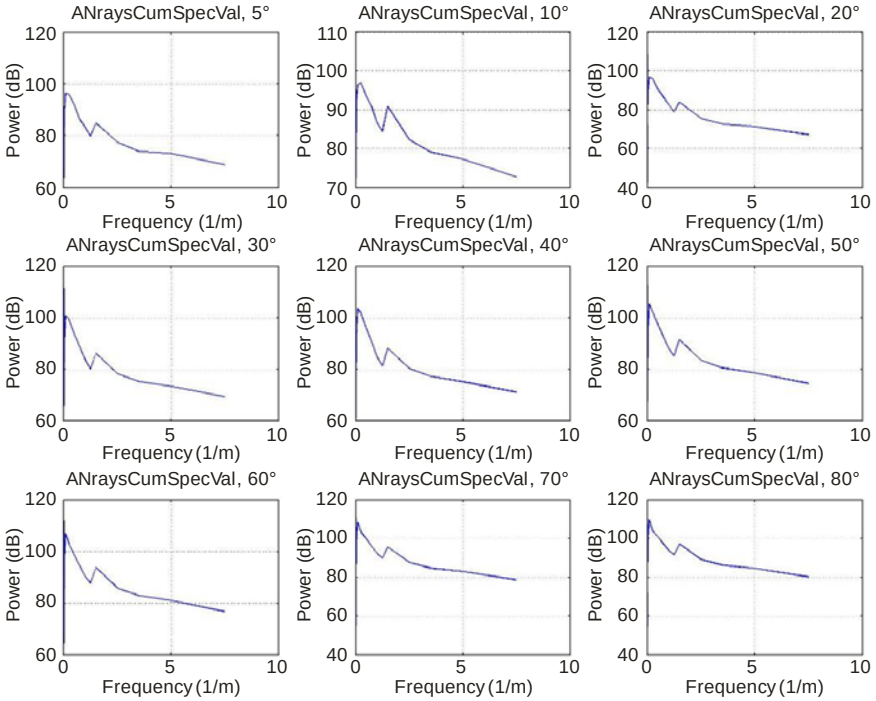

Report P.2145-38

4.2.2 Suburban vehicle

FIGURE 39

Probability density of a reflector being present at a horizontal position relative to the receiver

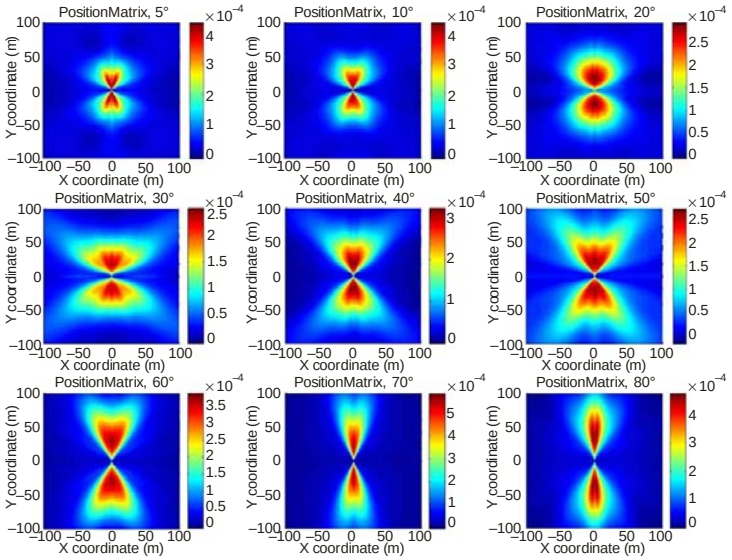

Report P.2145-39

FIGURE 40

Likelihood of a reflector being present at a certain relative azimuth angle between reflector and LoS

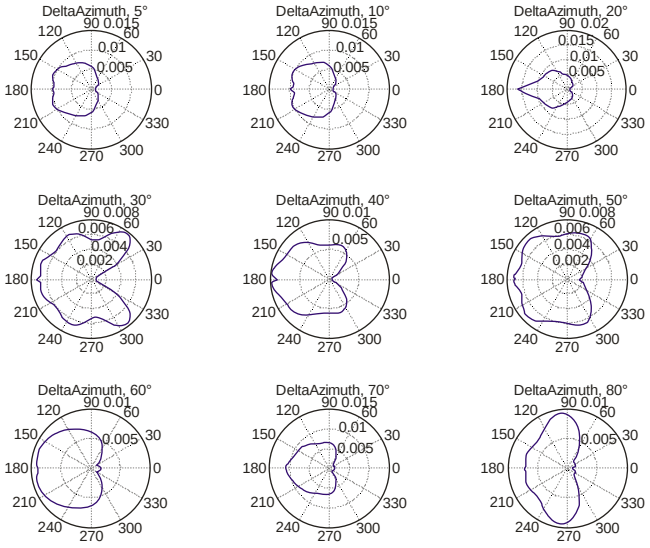

Report P. 2145-40

FIGURE 41

Mean power of a reflector for a certain horizontal position relative to the receiver

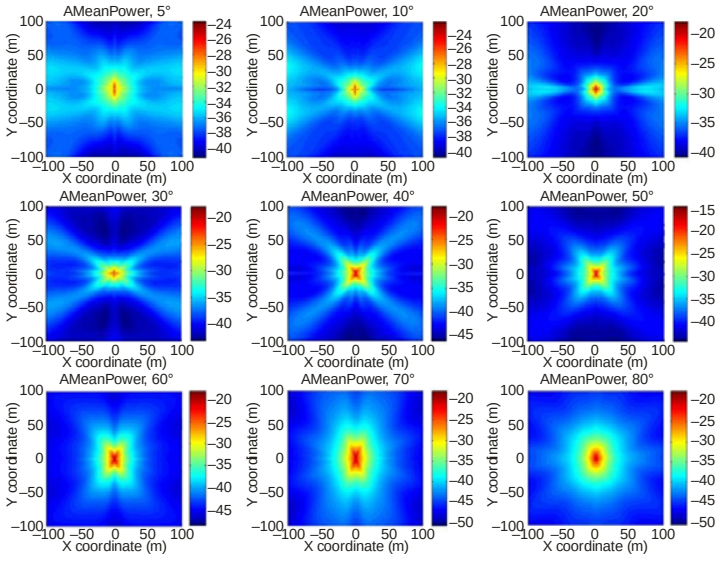

Report P. 2145-41

FIGURE 42

Standard deviation of the mean power of a reflector for a given relative horizontal position of a reflector

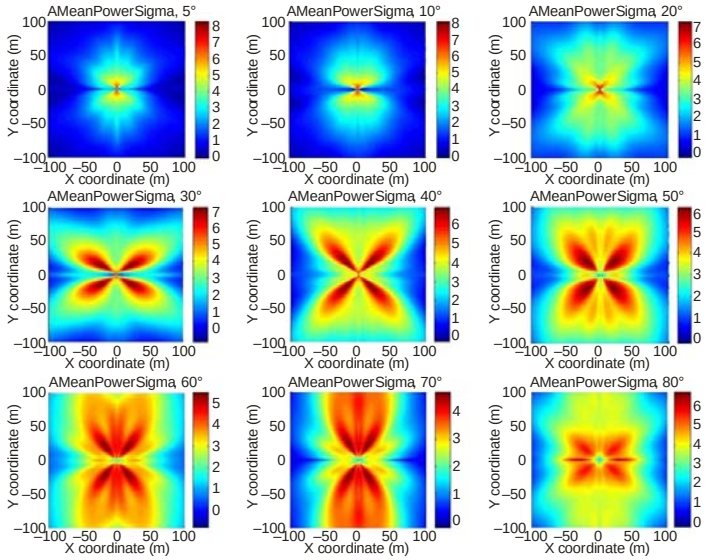

Report P.2145-42

FIGURE 43

Mean value of the bandwidth of an echo as a function of the satellite elevation

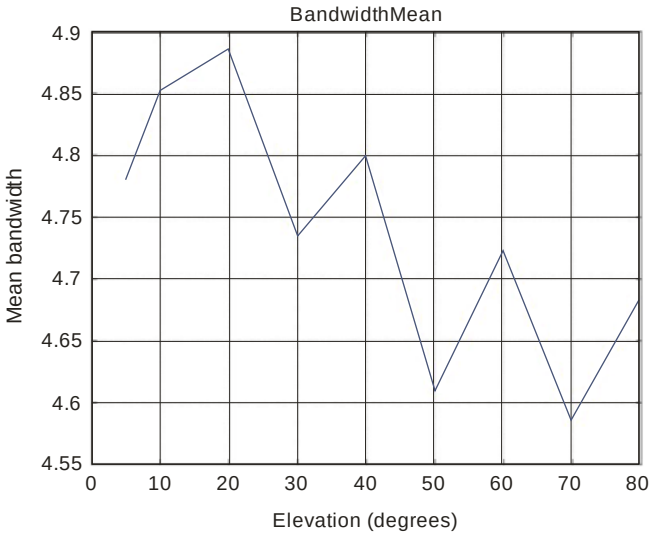

Report P.2145-43

FIGURE 44

Standard deviation of the bandwidth of an echo as a function of the elevation angle

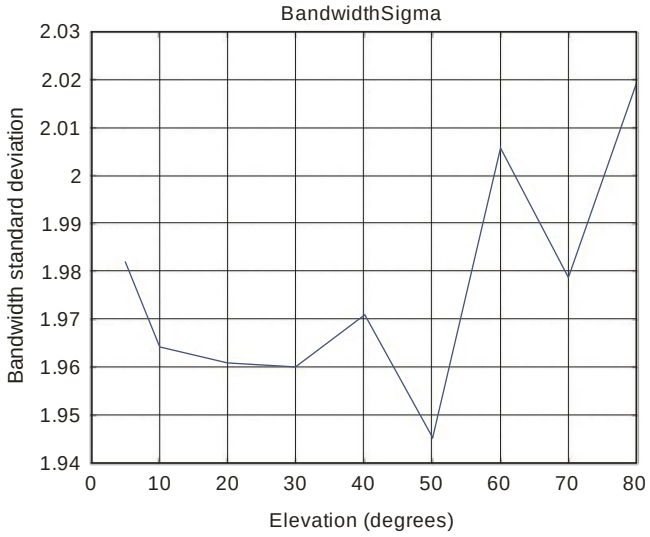

Report P.2145-44

FIGURE 45

Cumulative distribution function of the Rice factors as a function of the elevation angle

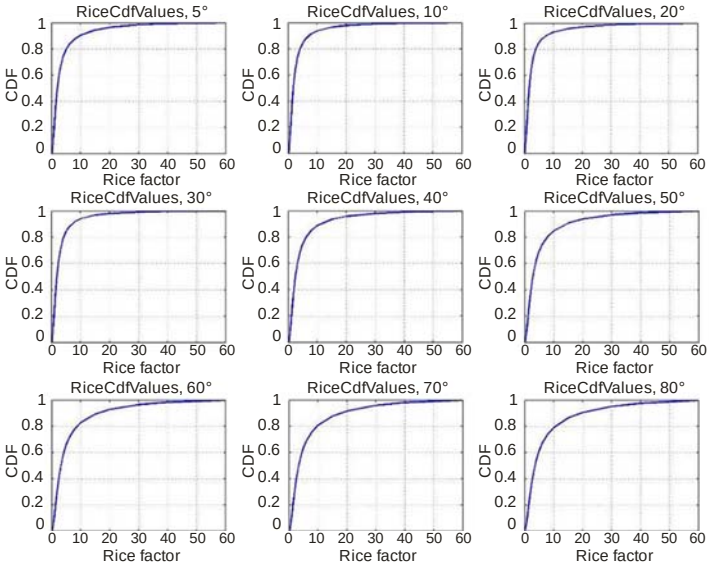

Report P.2145-45

FIGURE 46

Cumulative density function of the life span as a function of the elevation angle

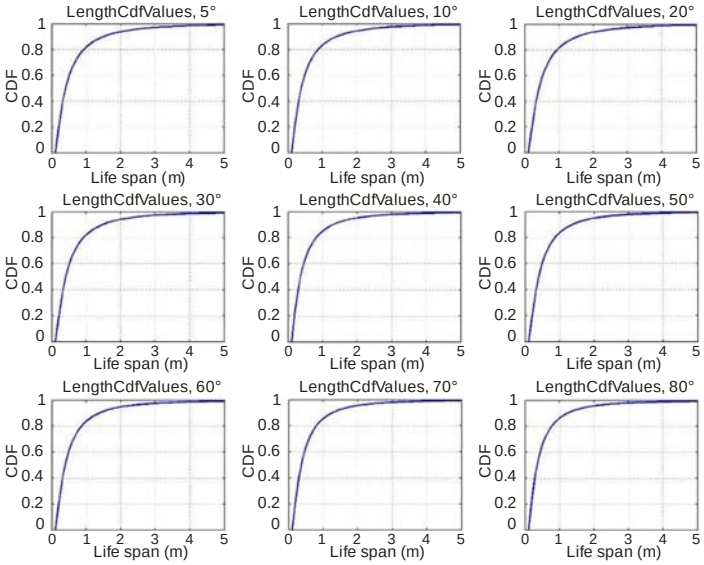

Report P. 2145-46

FIGURE 47

Probability that a reflector is moving in the same direction as the receiver as a function of the elevation angle

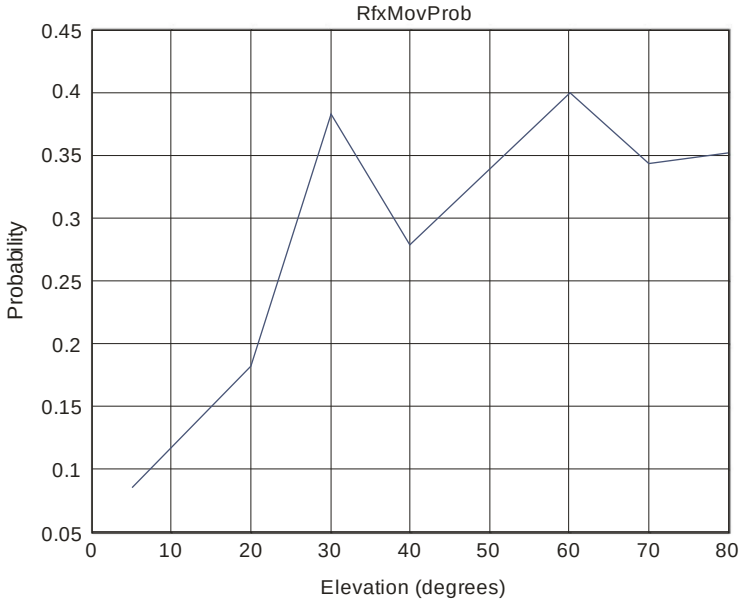

Report P. 2145-47

FIGURE 48

Mean number of coexisting reflectors as a function of the elevation angle

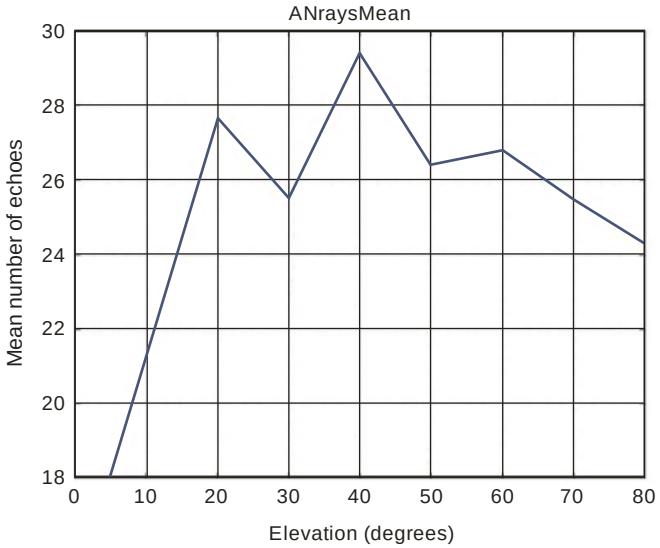

Report P.2145-48

FIGURE 49

Spectrum of the variation of the number of echoes over distance travelled in the x direction

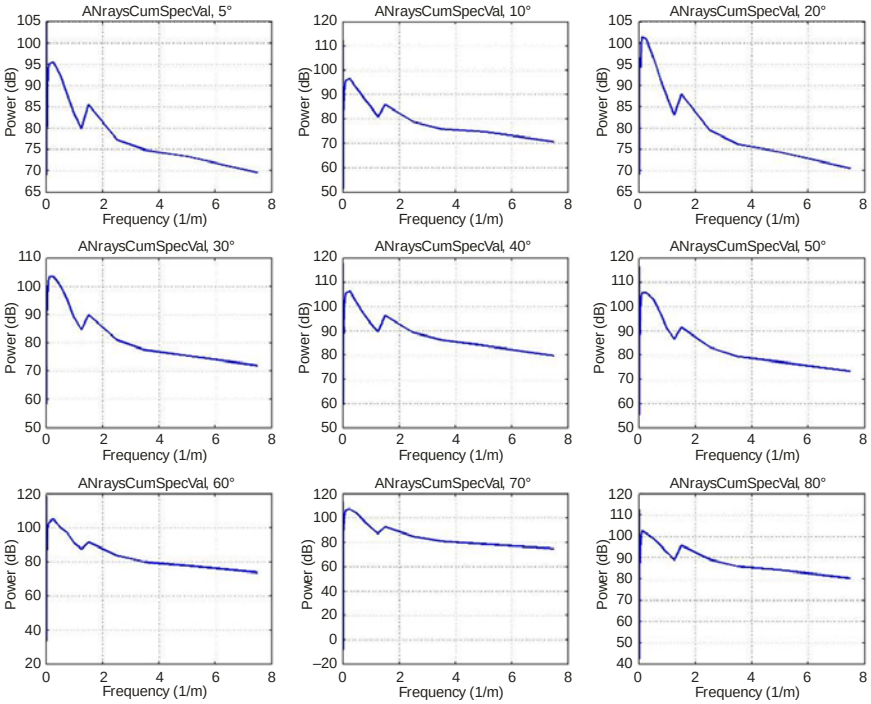

Report P.2145-49

4.2.3 Urban pedestrian

FIGURE 50

Probability density of a reflector being present at a horizontal position relative to the receiver

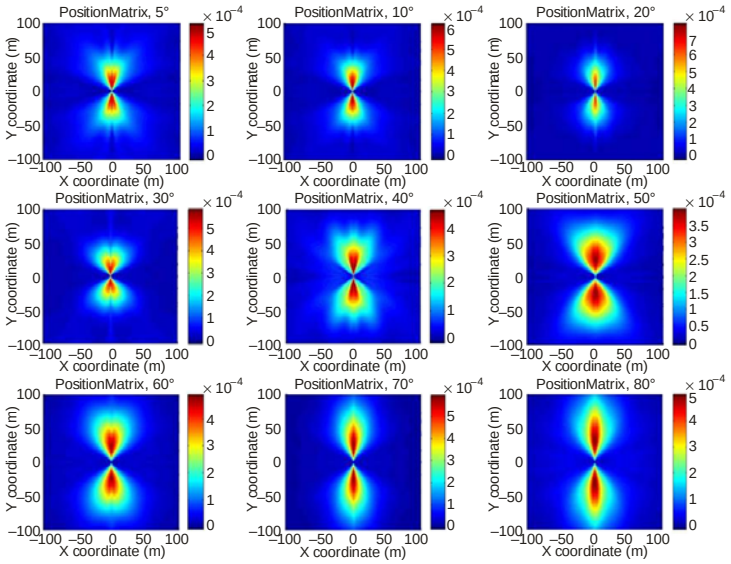

Report P.2145-50

FIGURE 51

Likelihood of a reflector being present at a certain relative azimuth angle between reflector and LoS

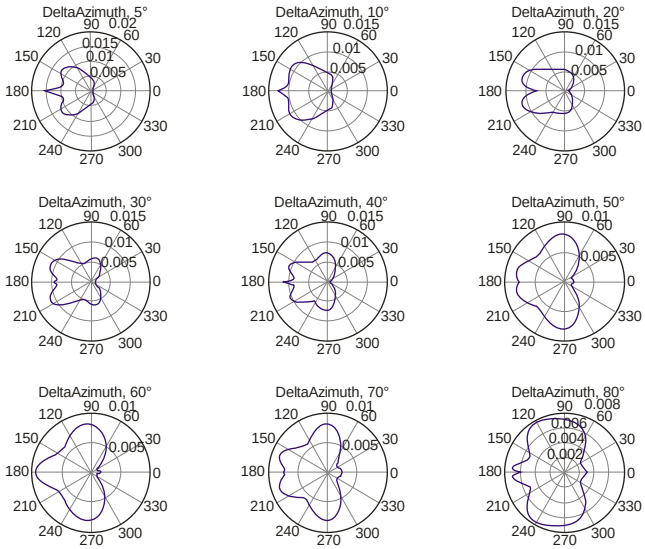

Report P.2145-51

FIGURE 52

Mean power of a reflector for a certain horizontal position relative to the receiver

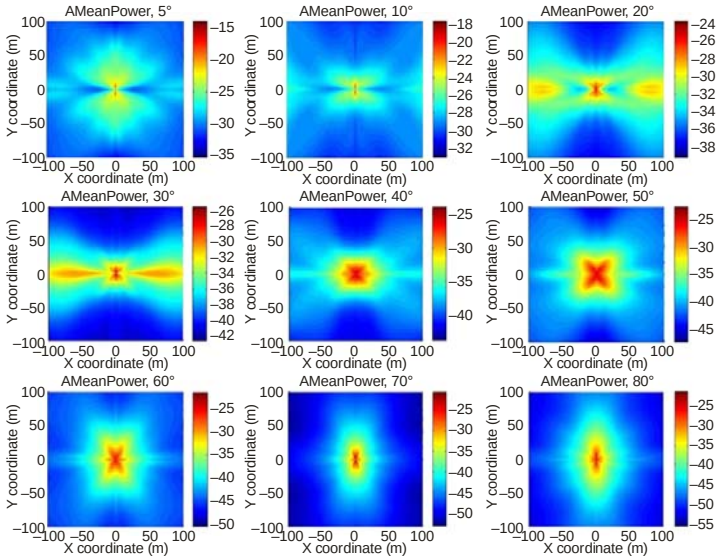

Report P.2145-52

FIGURE 53

Standard deviation of the mean power of a reflector for a given relative horizontal position of a reflector

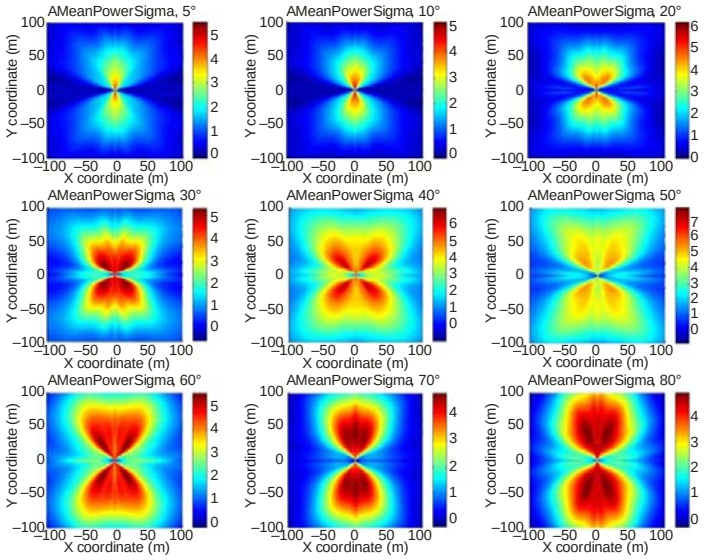

Report P.2145-53

FIGURE 54

Mean value of the bandwidth of an echo as a function of the satellite elevation

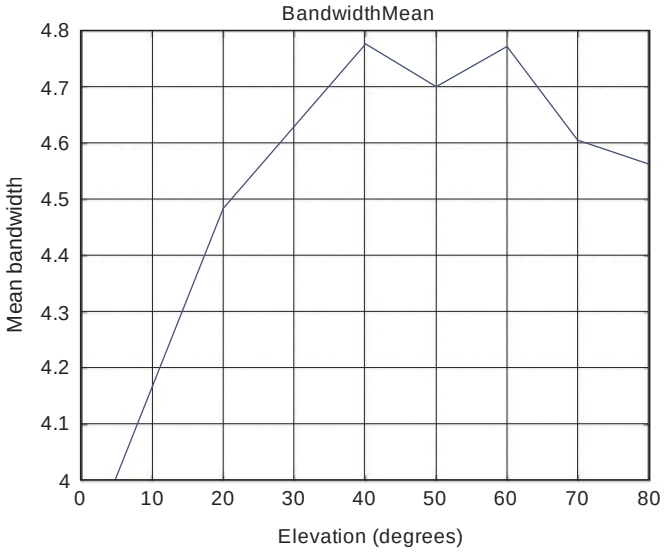

Report P.2145-54

FIGURE 55

Standard deviation of the bandwidth of an echo as a function of the elevation angle

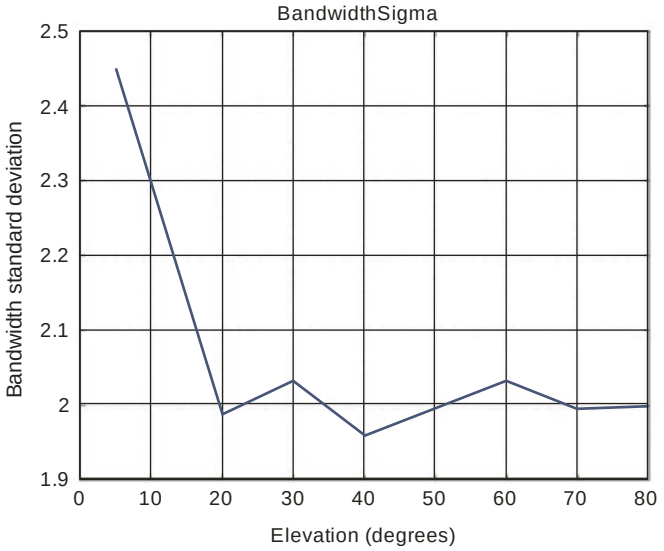

Report P.2145-55

FIGURE 56

Cumulative distribution function of the Rice factors as a function of the elevation angle

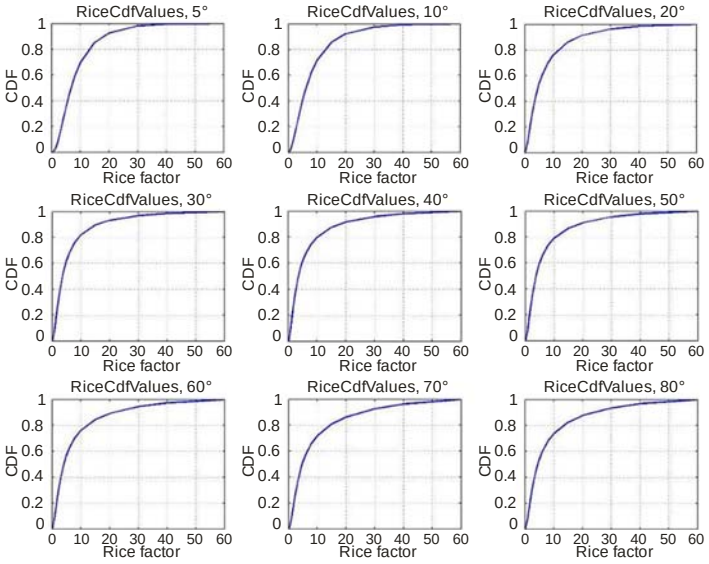

Report P. 2145-56

FIGURE 57

Cumulative density function of the life span as a function of the elevation angle

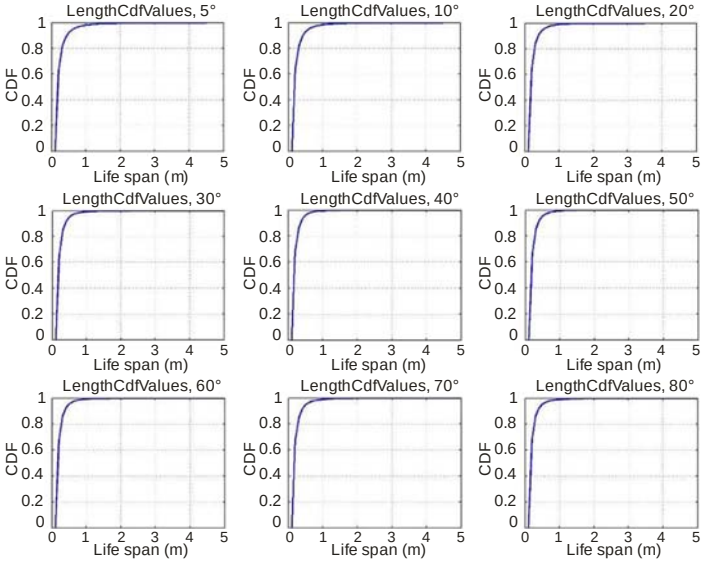

Report P. 2145-57

FIGURE 58

Probability that a reflector is moving in the same direction as the receiver as a function of the elevation angle

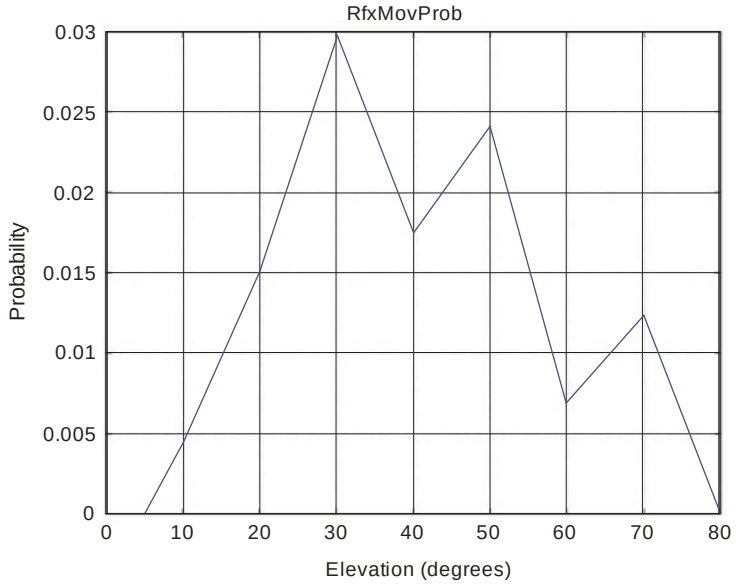

Report P. 2145-58

FIGURE 59

Mean number of coexisting reflectors as a function of the elevation angle

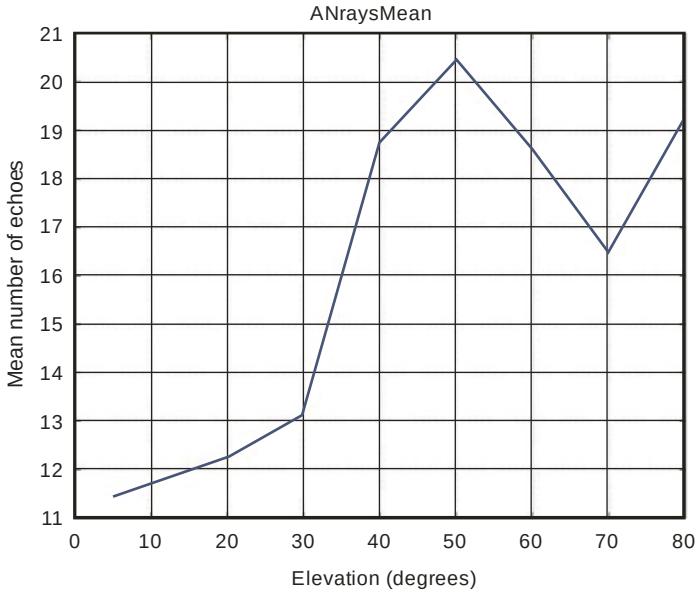

Report P. 2145-59

FIGURE 60

Spectrum of the variation of the number of echoes over distance travelled in the x direction

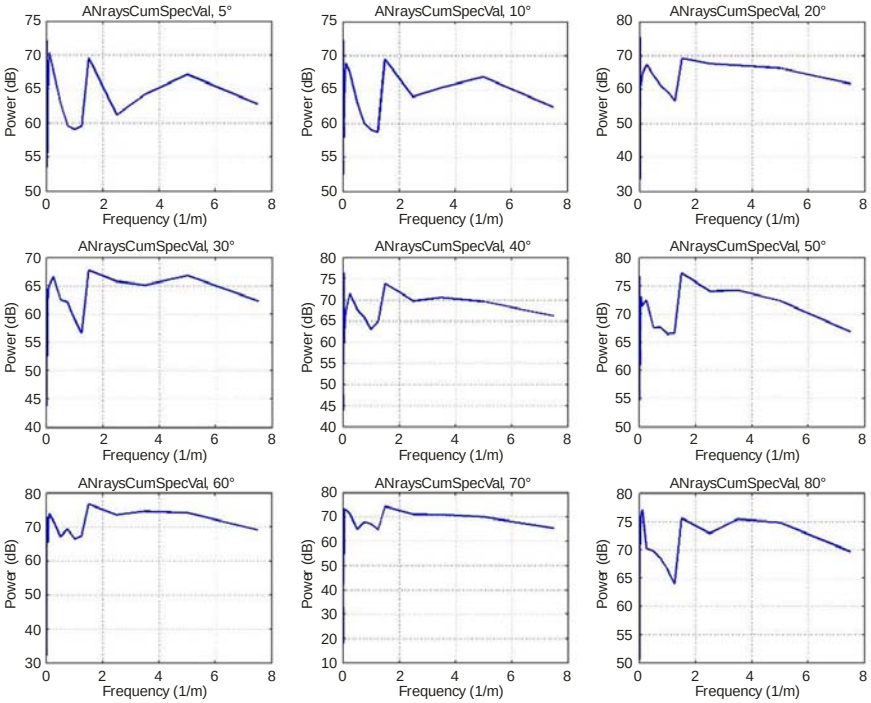

Report P. 2145-60

4.2.4 Suburban pedestrian

FIGURE 61

Probability density of a reflector being present at a horizontal position relative to the receiver

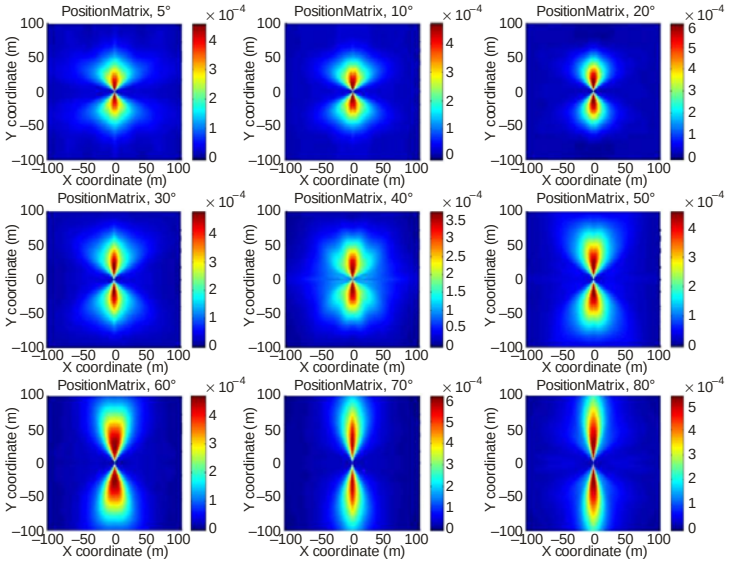

Report P. 2145-61

FIGURE 62

Likelihood of a reflector being present at a certain relative azimuth angle between reflector and LoS

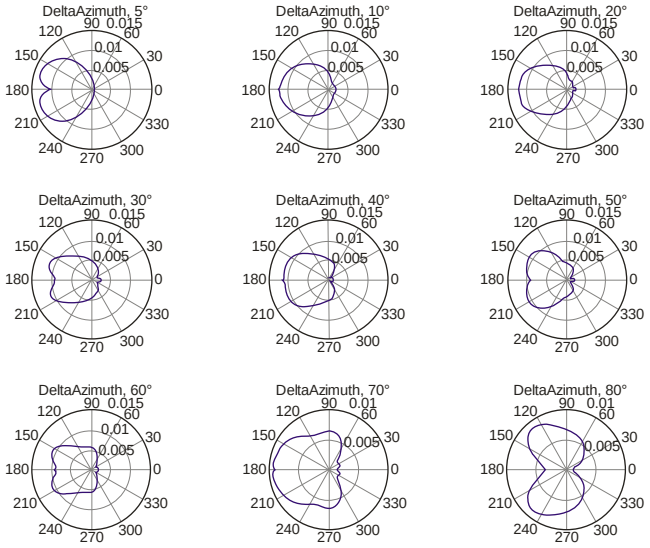

Report P.2145-62

FIGURE 63

Mean power of a reflector for a certain horizontal position relative to the receiver

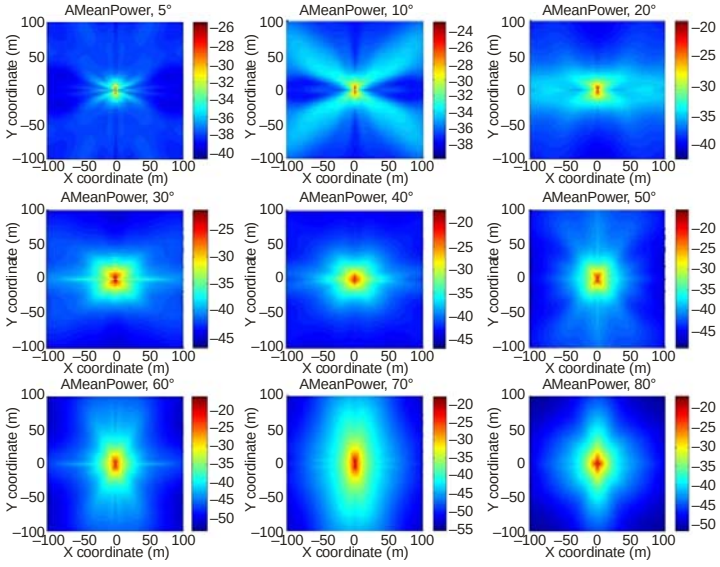

Report P.2145-63

FIGURE 64

Standard deviation of the mean power of a reflector for a given relative horizontal position of a reflector

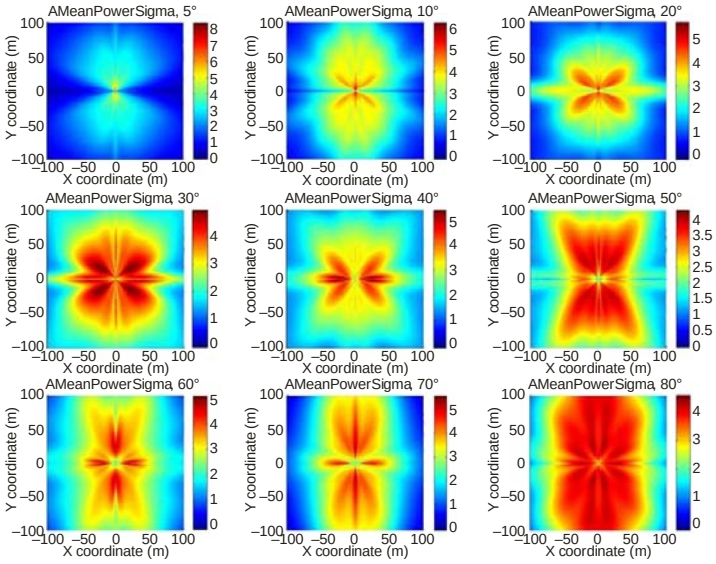

Report P. 2145-64

FIGURE 65

Mean value of the bandwidth of an echo as a function of the satellite elevation

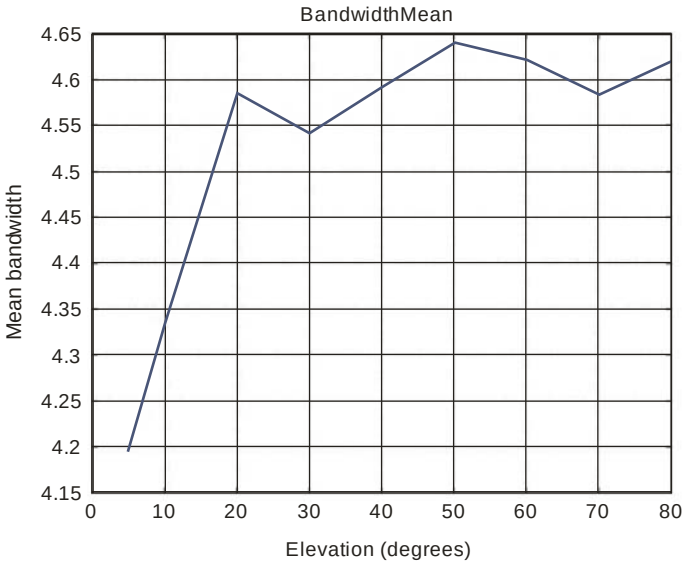

Report P. 2145-65

FIGURE 66

Standard deviation of the bandwidth of an echo as a function of the elevation angle

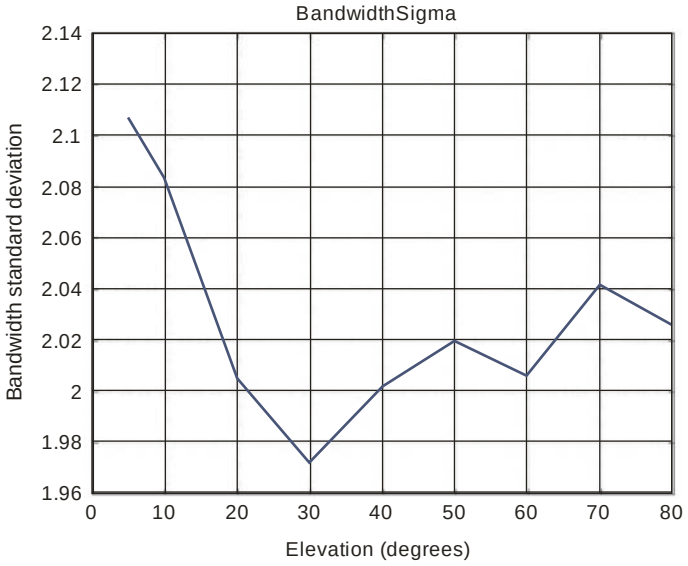

Report P.2145-66

FIGURE 67

Cumulative distribution function of the Rice factors as a function of the elevation angle

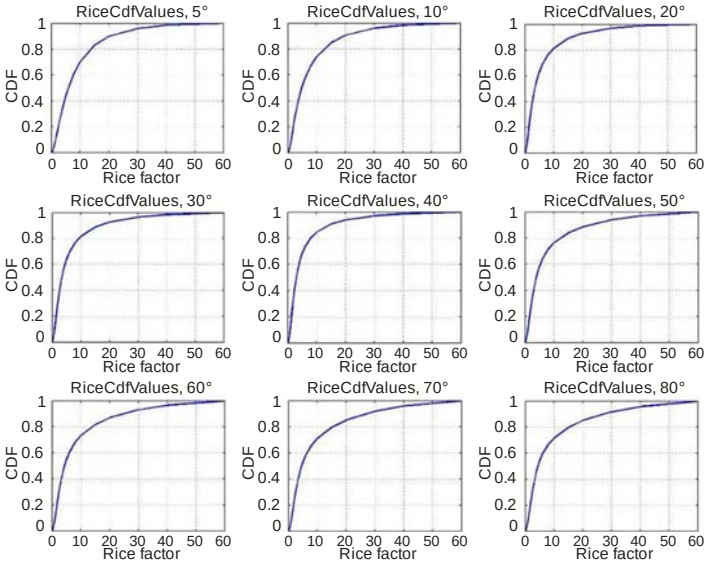

Report P.2145-67

FIGURE 68

Cumulative density function of the life span as a function of the elevation angle

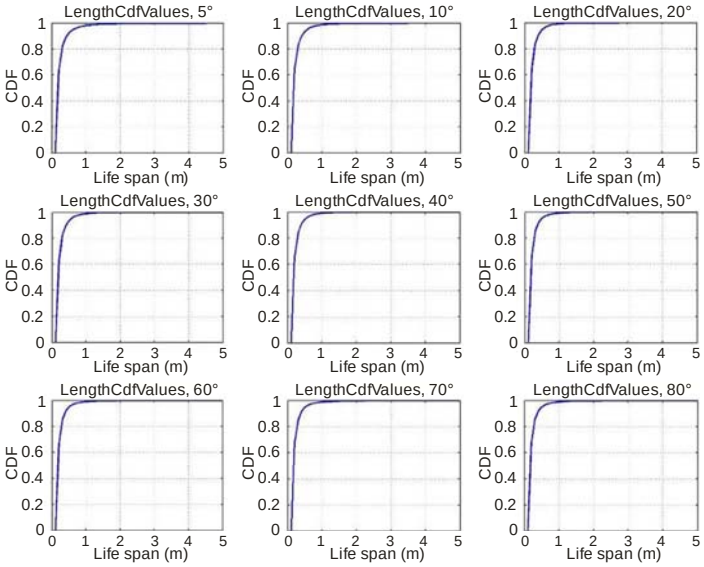

Report P. 2145-68

FIGURE 69

Probability that a reflector is moving in the same direction as the receiver as a function of the elevation angle

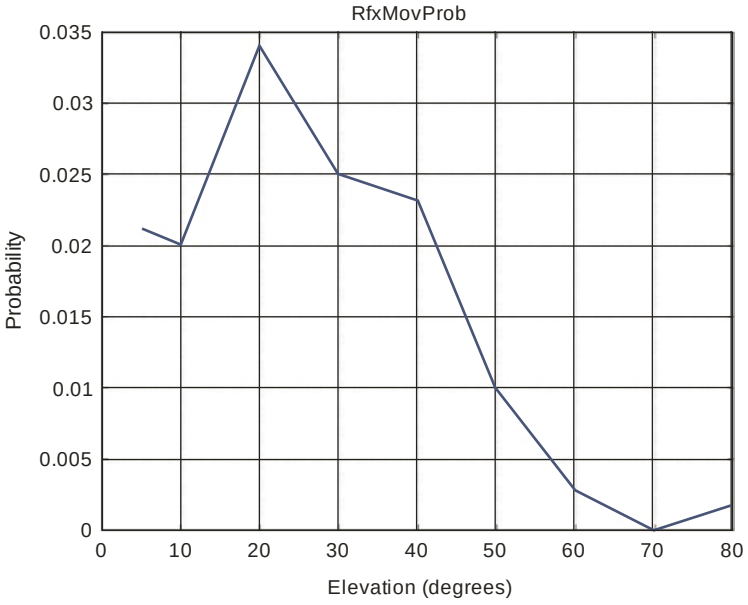

Report P. 2145-69

FIGURE 70

Mean number of coexisting reflectors as a function of the elevation angle

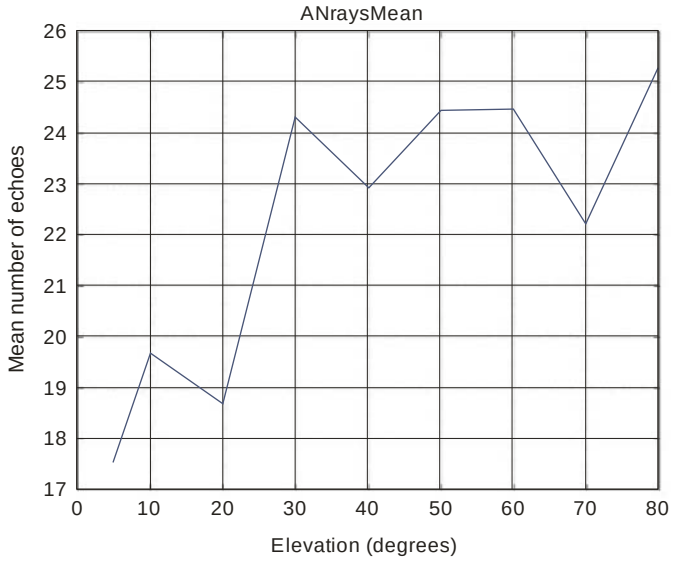

Report P.2145-70

FIGURE 71

Spectrum of the variation of the number of echoes over distance travelled in the x direction

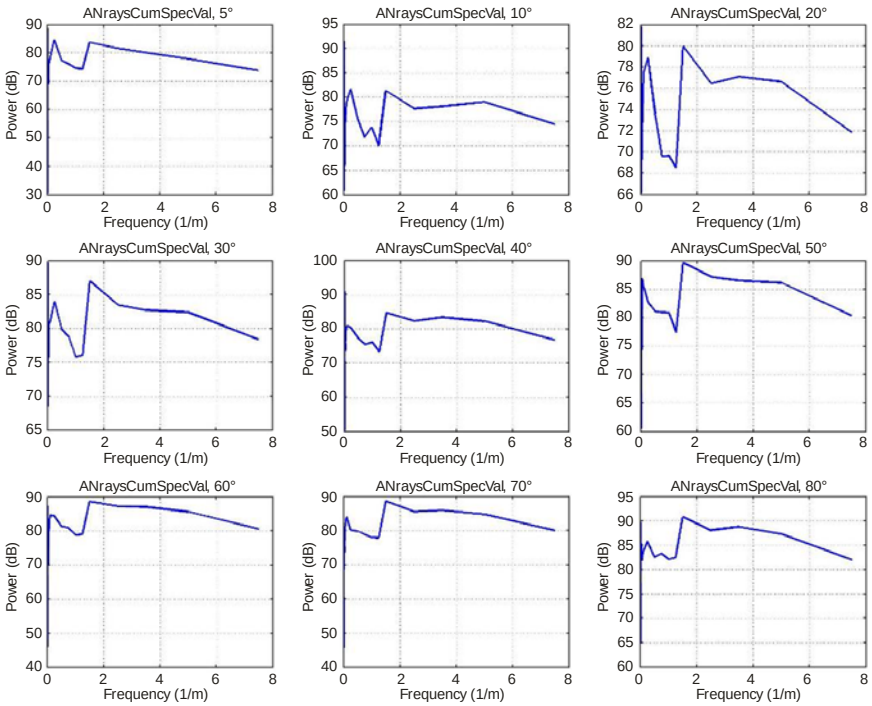

Report P.2145-71

4.3 Geometric parameters

Although any observed parameter set can be used to initialize this model, the following parameter settings are currently recommended. These values have been derived from observations in Munich (Germany).

4.3.1 User parameters

Urban vehicle

DistanceFromRoadMiddle	m	−5

Suburban vehicle

DistanceFromRoadMiddle	m	–2

Urban pedestrian

DistanceFromRoadMiddle	m	–6.5

Suburban pedestrian

DistanceFromRoadMiddle	m	–5.5

FIGURE 72

User parameters and antenna placement

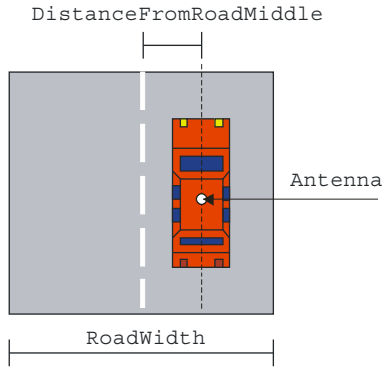

Report P. 2145-72

4.3.2 Building parameters

The building parameters set up the deterministic and statistical processes with respect to building shaping and placement. There are two rows of buildings that can be switched on. The building rows can be specified by a shaping process for house width and house height, and a placement process, which is governed by a gap-placing process. The Y-distance of the building rows is a fixed deterministic value.

Urban vehicle

BuildingRow1YPosition	m	−12
BuildingRow2YPosition	m	12
HouseWidthMean	m	22
HouseWidthSigma	m	25
HouseWidthMin	m	10
HouseHeightMean	m	16
HouseHeightSigma	m	6.4
HouseHeightMin	m	4
HouseHeightMax	m	50
GapWidthMean	m	27
GapWidthSigma	m	25
GapWidthMin	m	10
Gap Likelihood		0.18

Suburban vehicle

BuildingRow1YPosition	m	−7
BuildingRow2YPosition	m	7
HouseWidthMean	m	16
HouseWidthSigma	m	11
HouseWidthMin	m	5
HouseHeightMean	m	10
HouseHeightSigma	m	3.6
HouseHeightMin	m	3
HouseHeightMax	m	15
GapWidthMean	m	15
GapWidthSigma	m	22
GapWidthMin	m	2
Gap Likelihood		0.28

Urban pedestrian

BuildingRow1YPosition	m	−8
BuildingRow2YPosition	m	8
HouseWidthMean	m	22
HouseWidthSigma	m	25
HouseWidthMin	m	10
HouseHeightMean	m	16
HouseHeightSigma	m	6.4
HouseHeightMin	m	4
HouseHeightMax	m	50
GapWidthMean	m	27
GapWidthSigma	m	25
GapWidthMin	m	10
Gap Likelihood		0.18

Suburban pedestrian environment

BuildingRow1YPosition	m	7
BuildingRow2YPosition	m	7
HouseWidthMean	m	16
HouseWidthSigma	m	11
HouseWidthMin	m	5
HouseHeightMean	m	10
HouseHeightSigma	m	3.6
HouseHeightMin	m	3
HouseHeightMax	m	15
GapWidthMean	m	15
GapWidthSigma	m	22
GapWidthMin	m	2
Gap Likelihood		0.28

FIGURE 73

Building placement

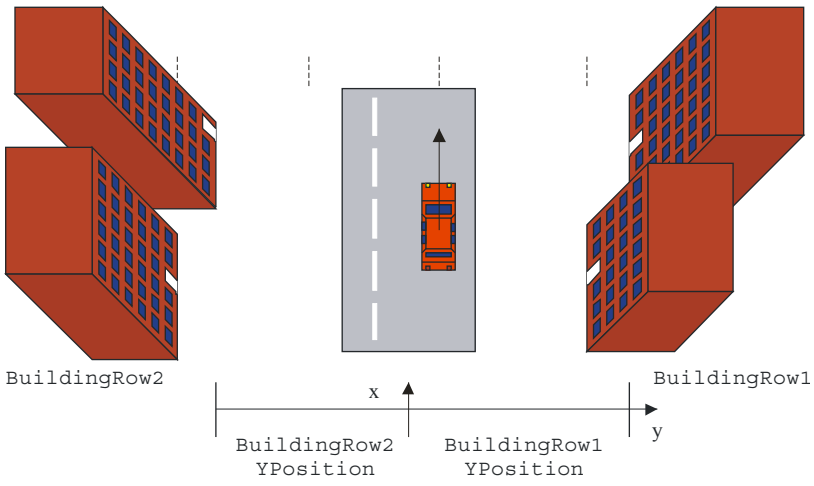

Report P.2145-73

FIGURE 74

Building shaping and placement processes

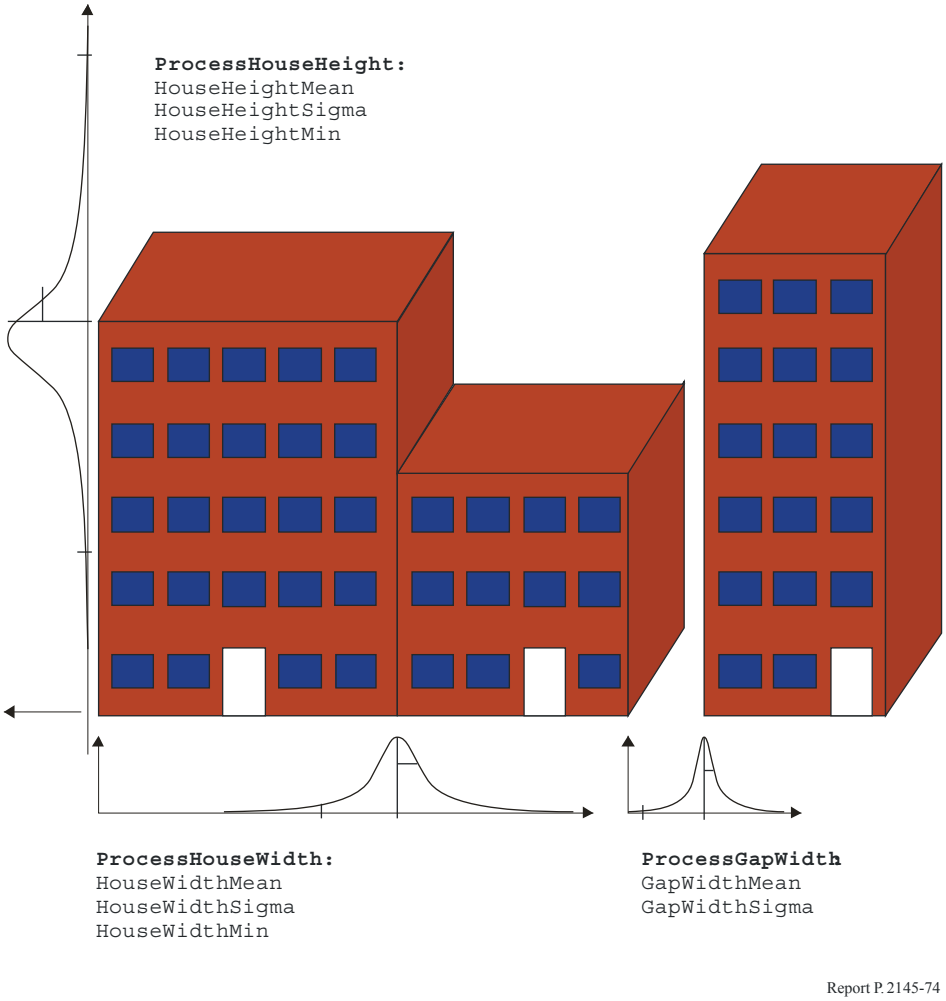

4.3.3 Tree parameters

Unlike the buildings, all trees in the scenario have the same deterministic shape. There are two rows of trees that can be switched on. The placement of both tree rows is controlled by separate statistical placement processes for each row, respectively.

Urban car environment

TreeHeight	m	8
TreeDiameter	m	5
TreeTrunkLength	m	2
TreeTrunkDiameter	m	0.2
TreeAttenuation	dB/m	1.1
TreeRow1YPosition	m	−8
TreeRow2YPosition	m	8
TreeRow1YSigma	m	2
TreeRow2YSigma	m	2
TreeRow1MeanDistance	m	60
TreeRow2MeanDistance	m	40
TreeRow1DistanceSigma	m	20
TreeRow2DistanceSigma	m	20

Suburban car environment

TreeHeight	m	7
TreeDiameter	m	4
TreeTrunkLength	m	2
TreeTrunkDiameter	m	0.2
TreeAttenuation	dB/m	1.1
TreeRow1YPosition	m	−5
TreeRow2YPosition	m	5
TreeRow1YSigma	m	0.5
TreeRow2YSigma	m	0.5
TreeRow1MeanDistance	m	40
TreeRow2MeanDistance	m	20
TreeRow1DistanceSigma	m	20
TreeRow2DistanceSigma	m	20

Urban pedestrian environment

TreeHeight	m	6
TreeDiameter	m	3
TreeTrunkLength	m	2
TreeTrunkDiameter	m	0.2
TreeAttenuation	dB/m	1.1
TreeRow1YPosition	m	−6
TreeRow2YPosition	m	6
TreeRow1YSigma	m	0.5
TreeRow2YSigma	m	0.5
TreeRow1MeanDistance	m	60
TreeRow2MeanDistance	m	40
TreeRow1DistanceSigma	m	20
TreeRow2DistanceSigma	m	20

Suburban pedestrian environment

TreeHeight	m	7
TreeDiameter	m	4
TreeTrunkLength	m	2
TreeTrunkDiameter	m	0.2
TreeAttenuation	dB/m	1.1
TreeRow1YPosition	m	−5
TreeRow2YPosition	m	5
TreeRow1YSigma	m	0.5
TreeRow2YSigma	m	0.5
TreeRow1MeanDistance	m	40
TreeRow2MeanDistance	m	20
TreeRow1DistanceSigma	m	20
TreeRow2DistanceSigma	m	20

FIGURE 75

Tree parameters

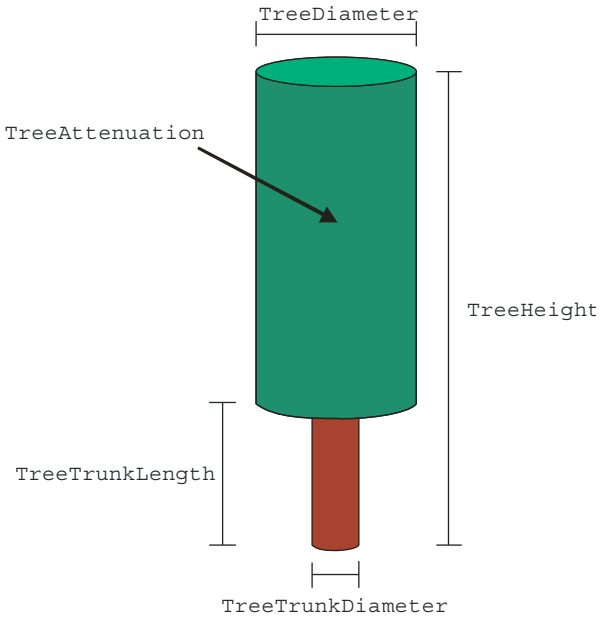

Report P.2145-75

FIGURE 76

Tree placement processes

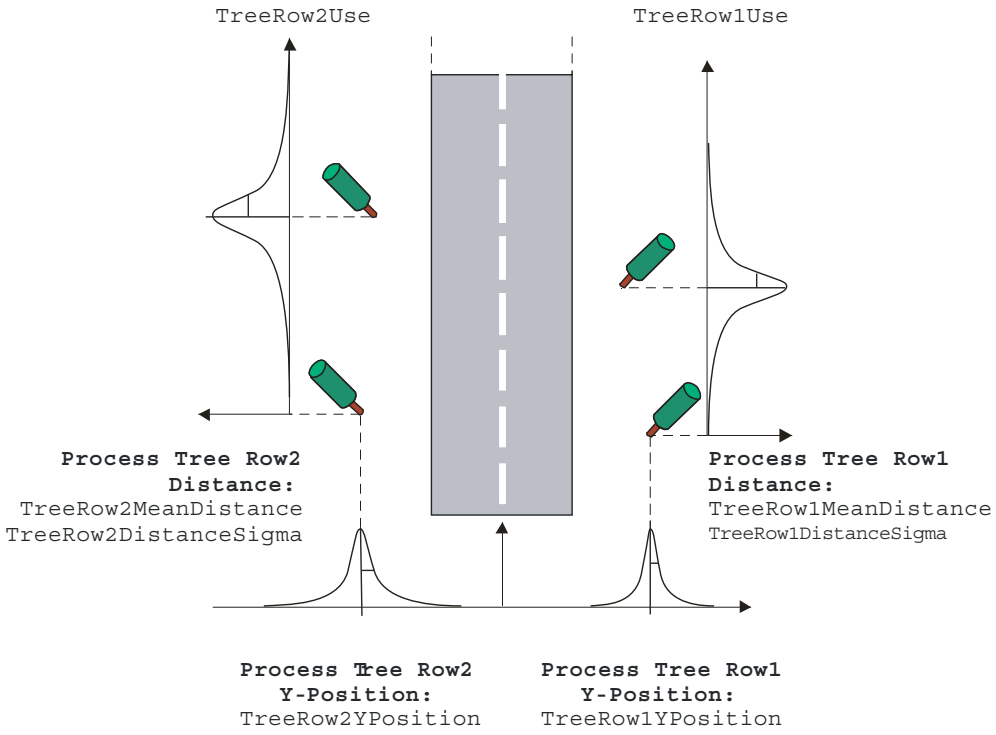

Report P.2145-76

4.3.4 Pole parameters

The handling of poles in the environment is similar to that for trees. The shape is the same for all poles, and there are two rows that can be switched on. The pole placement is likewise controlled by separate statistical placement processes.

Urban car environment

PoleRow1 use		Yes
Pole Row2 use		no
PoleHeight	m	10
PoleDiameter	m	0.2
PoleRow1YPosition	m	0
PoleRow2YPosition	m	10
PoleRow1YSigma	m	1
PoleRow2YSigma	m	1
PoleRow1MeanDistance	m	25
PoleRow2MeanDistance	m	10
PoleRow1DistanceSigma	m	10
PoleRow2DistanceSigma	m	10

Suburban car environment

PoleRow1 use		Yes
Pole Row2 use		no
PoleHeight	m	9
PoleDiameter	m	0.2
PoleRow1YPosition	m	0
PoleRow2YPosition	m	−5
PoleRow1YSigma	m	0.5
PoleRow2YSigma	m	0.5
PoleRow1MeanDistance	m	40
PoleRow2MeanDistance	m	40
PoleRow1DistanceSigma	m	5
PoleRow2DistanceSigma	m	5

Urban pedestrian environment

PoleRow1 use		Yes
Pole Row2 use		no
PoleHeight	m	10
PoleDiameter	m	0.2
PoleRow1YPosition	m	−6
PoleRow2YPosition	m	0
PoleRow1YSigma	m	0.5
PoleRow2YSigma	m	0.5
PoleRow1MeanDistance	m	25
PoleRow2MeanDistance	m	10
PoleRow1DistanceSigma	m	10
PoleRow2DistanceSigma	m	10

Suburban pedestrian environment

PoleRow1 use		Yes
Pole Row2 use		no
PoleHeight	m	9
PoleDiameter	m	0.2
PoleRow1YPosition	m	0
PoleRow2YPosition	m	−5
PoleRow1YSigma	m	0.5
PoleRow2YSigma	m	0.5
PoleRow1MeanDistance	m	40
PoleRow2MeanDistance	m	40
PoleRow1DistanceSigma	m	5
PoleRow2DistanceSigma	m	5

FIGURE 77

Pole parameters

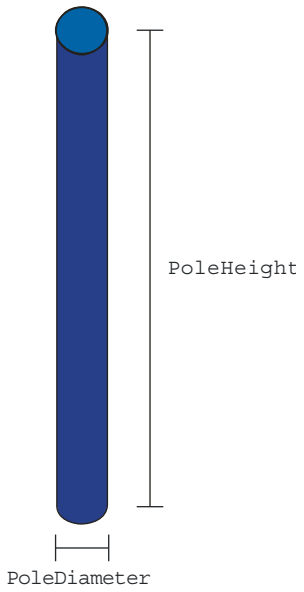

Report P.2145-77

FIGURE 78

Pole placement processes

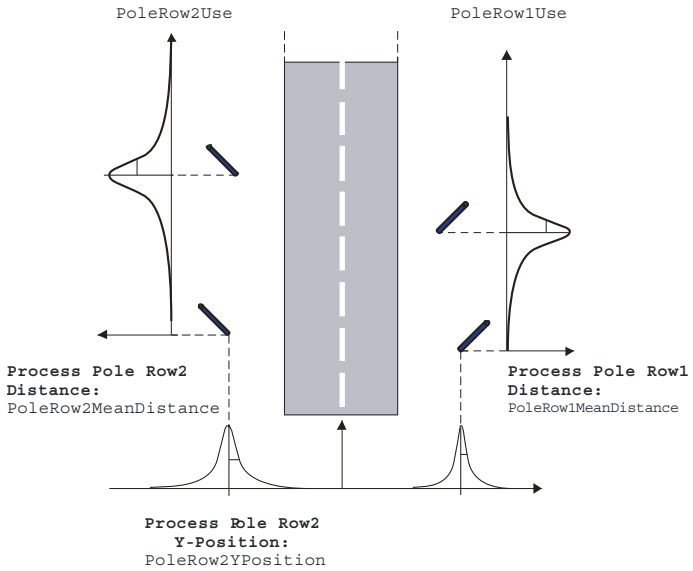

Report P.2145-78

5 Data file interface descriptions

This section contains information related to the software implementation of the LMSCM. It provides a description of the interface implemented in the software. The intention of this section is to allow a user of the software to use other statistical data than the one delivered with this implementation.

5.1 Statistical data file description

With the channel model implementation, two Matlab files which contain statistical channel data, are provided for different environments (urban, suburban) and different applications (car, pedestrian).

As example for car applications in an urban environment the statistical data files are named `EchoNumberParUrbanCar.mat` and `EchoParUrbanCar.mat`.

These two data files contain the following lists of Matlab variables:

```
EchoNumberParUrbanCar.mat
Name                       Size              Bytes  Class

ANraysCumSpecFreqBins     32x9                2304  double
ANraysCumSpecVal          32x9                2304  double
ANraysMean                 1x9                  72  double
ElevationVec               1x9                  72  double

EchoParUrbanCar.mat
Name                       Size              Bytes  Class

ABandwidthMean             1x9                  72  double
ABandwidthSigma            1x9                  72  double
ADeltaAzim                10x9                 720  double
ALengthCdfBins            24x9                1728  double
ALengthCdfValues          24x9                1728  double
AMeanPower                10x10x9             7200  double
AMeanPowerSigma           10x10x9             7200  double
APosition                 10x10x9             7200  double
ARfxMovProb                1x9                  72  double
ARiceCdfBins              27x9                1944  double
ARiceCdfValues            27x9                1944  double
ElevationVec               1x9                  72  double
```

5.1.1 Elevation vector

Different statistical channel parameters are stored in these variables. The last dimension of each variable is related to the satellite elevation, which is the angle between the tangential plane of the earth's surface at the user position and the incidence angle of the direct path signal from the satellite. Basis for the statistics are channel measurements at nine different elevations. These values are stored in the variable `ElevationVec` (degrees):

```
ElevationVec =

     5    10    20    30    40    50    60    70    80
```

5.1.2 Number of coexisting echoes

In the measurements a narrow and a wide band process were identified causing variations in the number of coexisting echoes as the receiver moves through the multipath environment. To model the receiver position dependent variations in the number of coexisting echoes $N_e(x)$, where x is the receiver's position along its trajectory, both processes are synthesized in the implemented channel model.

The discrete common CDF (Cumulative Distribution Function) of the narrow and wide band process is approximated by a piecewise linear function $P(X)$, which is stored in the variables `ANraysCumSpecVal` and `ANraysCumSpecFreqBins` for the nine different elevations.

As an example the values of the CDF with unit [1] for 5° elevation are:

```
ANraysCumSpecVal(:,1)' =

  1.0e+006 *

0    0.4294    0.4897    0.4970    0.5587    0.6614    0.7495
0.7734    0.7771    0.7795    0.7891    0.7911    0.7978
0.8025    0.8041    0.8138    0.8294    0.8440    0.8696
0.8841    0.9148    0.9805    1.0429    1.0813    1.1017
1.1160    1.1258    1.1431    1.1505    1.1555    1.1600
1.1627
```

at the corresponding spatial frequencies with unit [1/m] stored in:

```
ANraysCumSpecFreqBins(:,1)' =

0     0.0005    0.0010    0.0015    0.0020    0.0025    0.0030
0.0035     0.0040     0.0045     0.0055      0.0065    0.0075
0.0085     0.0095     0.0120     0.0145     0.0195     0.0345
0.0495     0.0995     0.2495     0.4995     0.7495     0.9995
1.2495     1.4995     2.4995     3.4995     4.9995     7.4995
9.9995
```

In the channel model the spectrum of the process is derived from the CDF $P(X)$ by differentiation. Next an inverse Fourier transform is calculated resulting in the synthesized change of the number of coexisting echoes $N_p(x)$. The total number of coexisting echoes is calculated by adding the average number of echoes $\bar{n}$ with a lower bound of zero:

$$N_e(x) = \max(0, N_p(x) + \bar{n})$$

The average number of coexisting echoes $\bar{n}$ is stored in the variable `ANraysMean`. As example, the values for the different elevations in the urban environment for car applications are:

```
ANraysMean =

 8.7311     13.0396   13.2762   18.3764   23.4766   24.6038
25.7309   26.8581   27.9853
```

5.2 Echo bandwidth

In the implemented model the distribution of the echoes' bandwidth is modelled by a Gaussian process. The corresponding mean and variance values in Hz are stored in the variables `ABandwidthMean` and `ABandwidthSigma` for the different elevations. Again for the urban car example these values are:

```
ABandwidthMean =
4.6770    4.6874    4.6990    4.7520    4.8049    4.7791
4.7533    4.7275    4.7017
```

and

```
ABandwidthSigma =

2.0850      2.0817      2.0652    2.0271    1.9889    1.9829
1.9769      1.9709      1.9649
```

5.3 Life span of reflectors

In the measurement data the channel appears rapidly changing. Many echoes disappear and new ones appear. This process is highly correlated to the receiver speed. When the receiver stops, the echoes remain. In order to allow the motion dependent modelling of the multipath channel, the echo life span in meters is defined. This life span is the distance the receiver is travelling from appearance of an echo until it disappears.

The discrete distribution of the life span of reflectors, respectively its CDF, is stored in the variables `ALengthCdfBins` and `ALengthCdfValues`, where for example:

```
ALengthCdfValues(:,1)' =
0    0.2776    0.4758    0.6044    0.6934    0.7568    0.8030
0.8373    0.8637    0.8844    0.9144    0.9348    0.9492
0.9598    0.9675    0.9798    0.9866    0.9934    0.9963
0.9977    0.9990    0.9994    0.9999    1.0000
```

are the values at the lowest elevation of 5° at the corresponding life spans (m):

```
ALengthCdfBins(:,1)' =
0.1000    0.2000    0.3000    0.4000    0.5000    0.6000
0.7000    0.8000    0.9000    1.0000    1.2000    1.4000
1.6000    1.8000    2.0000    2.5000    3.0000    4.0000
5.0000    6.0000    8.0000   10.0000   15.0000   20.0000
```

5.4 Rice factor of echoes

The fading characteristic of single echo signals observed in the measured data indicates a constant component. Therefore a Ricean model is applied. The discrete distribution of the Rice factors of echo signals, respectively its CDF, is stored in the variables `ARiceCdfBins` and `ARiceCdfValues`, where for example:

```
ARiceCdfValues(:,1)' =

0    0.0058    0.0138    0.0220    0.0313    0.0422    0.0542
0.0672    0.0810    0.0955    0.1255    0.1561    0.1864
0.2161    0.2448    0.3109    0.3686    0.4645    0.5412
0.6027    0.6937    0.7579    0.8538    0.9042    0.9553
0.9799    1.0000
```

are the values at the lowest elevation of 5° at the corresponding Rice factor bins

```
ARiceCdfBins(:,1)' =

0.1000    0.2000    0.3000    0.4000    0.5000    0.6000
0.7000    0.8000    0.9000    1.0000    1.2000    1.4000
1.6000    1.8000    2.0000    2.5000    3.0000    4.0000
5.0000    6.0000    8.0000   10.0000   15.0000   20.0000
30.0000   40.0000   60.0000
```

5.5 Movement of reflection points

The measurements also revealed that some reflection points move according to the movement of the receiver (like e.g. on a house wall), while others remain at fixed positions. A measure for this behaviour is the observed change in the angle α, which is the angle between the van's moving direction and the direction to the reflection point. For a theoretically fixed reflection α would change according to the movement of the receiver. On the other hand, if the reflection point moves e.g. along a house front, α does not change during the observation interval. The distribution of this angular changes shows a significant bend, which allows to estimate the percentage of reflection points which are moving. The rest can be associated with fixed reflectors, e.g., traffic signs or trees, which in general have very short life spans.

The probabilities for a moving reflection point at different elevations are stored in:

```
ARfxMovProb =

0.0209    0.0387    0.0559    0.1386    0.1471    0.1536
0.1600    0.1665    0.1730
```

5.6 Horizontal reflector position distribution

Further analysis of the measurement data show, that the horizontal position distribution of reflectors relative to the receiver position changes significantly for different elevations. These two-dimensional distributions are symmetrical with respect to the movement direction of the receiver, because in urban and suburban environments the likelihood for a reflector to be on the left or the right side of a street is the same. Moreover, the likelihood for a reflector in front or in the rear is the same, thus the distributions are symmetrical with respect to the cross axis, too. Hence, only a quarter of the distributions needs to be stored.

The two-step polynomial approximations of these horizontal reflector position distributions are stored in the variable APosition.

As an example the polynomial coefficients for 5° elevation in the urban car case are:

```
APosition(:,:,1) =

  Columns 1 through 4

 -4.2762e-038  8.4117e-035 -6.9855e-032  3.1800e-029
  1.9300e-035 -3.7787e-032  3.1218e-029 -1.4130e-026
 -3.6100e-033  7.0363e-030 -5.7842e-027  2.6030e-024
  3.6015e-031 -6.9922e-028  5.7219e-025 -2.5610e-022
 -2.0482e-029  3.9650e-026 -3.2331e-023  1.4405e-020
  6.5416e-028 -1.2655e-024  1.0305e-021 -4.5796e-019
 -1.0705e-026  2.0804e-023 -1.7004e-020  7.5746e-018
  7.3129e-026 -1.4463e-022  1.2015e-019 -5.4257e-017
 -6.1199e-026  1.3699e-022 -1.2466e-019  5.9536e-017
  4.5639e-025 -9.4822e-022  8.3410e-019 -4.0362e-016
```

```
  Columns 5 through 8

 -8.6107e-027  1.4025e-024 -1.3089e-022  5.9626e-021
  3.8008e-024 -6.1448e-022  5.6899e-020 -2.5789e-018
 -6.9548e-022  1.1153e-019 -1.0229e-017  4.5915e-016
  6.7969e-020 -1.0807e-017  9.7998e-016 -4.3308e-014
 -3.7995e-018  5.9880e-016 -5.3581e-014  2.3133e-012
  1.2024e-016 -1.8796e-014  1.6558e-012 -6.9005e-011
 -1.9881e-015  3.0896e-013 -2.6721e-011  1.0509e-009
  1.4368e-014 -2.2300e-012  1.8771e-010 -6.5134e-009
 -1.5862e-014  2.2390e-012 -1.1857e-010 -5.9136e-009
  1.1683e-013 -2.0590e-011  2.1473e-009 -1.2071e-007


  Columns 9 through 10

 -6.7635e-020 -8.6843e-019
  3.0199e-017  3.4464e-016
 -5.3951e-015 -5.9065e-014
  4.9353e-013  5.7003e-012
 -2.4271e-011 -3.3547e-010
  5.9928e-010  1.2058e-008
 -5.2603e-009 -2.5004e-007
 -3.0846e-008  2.7240e-006
  7.7678e-007 -1.2097e-005
  2.6144e-006  3.7349e-005
```

In the model a quarter of the horizontal reflector position distribution in polar coordinates is calculated from these coefficients by:

```
for
r = 1:length(RadiusVec)
p = diag(APosition(:,:,k)*repmat([RadiusVec(r).^[9:-1:0]],11,1)');
y = polyval(p(1:10),AzimuthVec,9);
A(:,r) = y';                    % Quarter of position distribution
end
```

where *k* is the index of the elevation and:

```
RadiusVec = [0:2:250];          % Model radius grid in m
AzimuthVec = [0:2:90];          % Model azimuth grid in degrees
```

5.7 The relative satellite-reflector azimuth angle

The above described horizontal reflector position distributions are independent of the satellite azimuth. In order to model the multipath channel dependent on both satellite elevation and azimuth, statistics for the azimuthal angle of arrival of echoes relative to the LoS signal are used. As the measurements revealed these distributions are symmetrical for positive and negative angles.

Polynomial approximations of these statistics between 0-180° (because of the symmetry) are stored in the variable `ADeltaAzim` for the different elevation angles. As example for 5° elevation in the urban car case the polynomial coefficients are:

```
ADeltaAzim(:,1)' =

-6.6625e-020  5.8308e-017 -2.1039e-014  4.0321e-012 -4.4015e-
010   2.7190e-008 -8.8648e-007  1.3628e-005 -6.6625e-005
9.9306e-004
```

In the model the relative satellite-reflector azimuth angle distribution is calculated from these coefficients by:

```
A = polyval(ADeltaAzim(:,k),DeltaAzimuthVec,9);
Afull = [A,A(end-1:-1:1)];   % Full delta azimuth distribution
```

where *k* is the index of the elevation and:

```
DeltaAzimuthVec = [0:2:180]; % Model delta azimuth grid in degrees
```

5.8 Average power of echo signals

The distance and direction of a reflector from the receiver plays a major role for the power of the received echo signal. This fact is taken into account in the LMS channel model. From the measurement data statistics for the mean and for the standard deviation of the average echo power depending on the relative horizontal reflector position were determined. Again these two-dimensional distributions are symmetrical with respect to the movement direction of the receiver and with respect to the cross axis. Hence, only a quarter of the distributions needs to be stored.

The two step polynomial approximations of mean and variance of these echo power distributions are stored in the variables `AMeanPower` and `AMeanPowerSigma`, respectively. The mean and variance values of these distributions are giving the echo powers in dB relative to an unobstructed direct path signal.

```
AMeanPower(:,:,1) =

  Columns 1 through 4

  3.2415e-033 -4.4259e-030  2.0915e-027 -2.4915e-025
 -1.4516e-030  2.0161e-027 -9.8989e-025  1.4582e-022
  2.6687e-028 -3.7401e-025  1.8708e-022 -2.9970e-020
 -2.5852e-026  3.6192e-023 -1.8021e-020  2.8107e-018
  1.3999e-024 -1.9254e-021  9.1711e-019 -1.1130e-016
 -4.0648e-023  5.2756e-020 -2.1378e-017 -3.5833e-016
  4.9848e-022 -4.9793e-019  1.5104e-017  1.7251e-013
```

```
   1.2194e-021 -6.0663e-018  8.0632e-015 -5.0351e-012
  -6.4724e-020  1.2835e-016 -1.0736e-013  4.9239e-011
   1.1131e-019 -1.7655e-016  1.1110e-013 -3.4615e-011

   Columns 5 through 8

  -1.1925e-022  5.0124e-020 -7.8214e-018  5.5650e-016
   4.1637e-020 -2.0094e-017  3.2257e-015 -2.3139e-013
  -6.5995e-018  3.4849e-015 -5.6760e-013  4.0781e-011
   6.7858e-016 -3.4584e-013  5.5772e-011 -3.9715e-009
  -5.1674e-014  2.1765e-011 -3.3575e-009  2.3344e-007
   2.7945e-012 -8.9493e-010  1.2720e-007 -8.4755e-006
  -9.4727e-011  2.3281e-008 -2.9617e-006  1.8540e-004
   1.7310e-009 -3.4324e-007  3.8525e-005 -2.2248e-003
  -1.3471e-008  2.2365e-006 -2.1816e-004  1.1296e-002
   5.2379e-009 -2.3587e-007 -2.8721e-005  3.6428e-003

   Columns 9 through 10

  -1.4925e-014  1.0488e-013
   6.1936e-012 -4.3351e-011
  -1.0852e-009  7.5583e-009
   1.0450e-007 -7.2361e-007
  -6.0306e-006  4.1483e-005
   2.1307e-004 -1.4548e-003
  -4.4920e-003  3.0403e-002
   5.1368e-002 -3.4283e-001
  -2.4106e-001  1.5657e+000
  -1.4033e-001 -3.0032e+001

AMeanPowerSigma(:,:,1) =

   Columns 1 through 4

  -6.7162e-036 -1.3427e-031  2.5678e-028 -1.9790e-025
   2.8474e-032  8.2478e-030 -6.9534e-026  6.6278e-023
  -1.0421e-029  8.8194e-027  3.9699e-024 -7.9929e-021
   1.6298e-027 -2.0585e-024  6.0874e-022  3.2146e-019
  -1.3599e-025  2.0158e-022 -1.0457e-019  1.3616e-017
   6.4285e-024 -1.0401e-020  6.5078e-018 -1.8134e-015
  -1.7047e-022  2.9095e-019 -1.9957e-016  6.8149e-014
   2.3556e-021 -4.1320e-018  2.9566e-015 -1.0897e-012
  -1.4295e-020  2.4816e-017 -1.7517e-014  6.3391e-012
   5.5300e-020 -9.8571e-017  7.2827e-014 -2.8728e-011

   Columns 5 through 8

   8.1771e-023 -1.9705e-020  2.8014e-018 -2.2505e-016
  -2.9883e-020  7.5472e-018 -1.1046e-015  9.0513e-014
   4.2796e-018 -1.1681e-015  1.7878e-013 -1.5090e-011
  -2.9039e-016  9.2293e-014 -1.5227e-011  1.3459e-009
   7.8105e-015 -3.8059e-012  7.2537e-010 -6.9179e-008
```

```
  1.0264e-013  6.8814e-011 -1.8867e-008  2.0593e-006
 -1.0763e-011  5.6750e-011  2.4039e-007 -3.4208e-005
  2.0843e-010 -1.4956e-008 -1.3074e-006  3.0631e-004
 -1.1794e-009  7.9272e-008  7.7429e-006 -1.6358e-003
  6.4736e-009 -8.1970e-007  5.1574e-005 -8.2620e-004

  Columns 9 through 10

  8.9018e-015 -9.8528e-014
 -3.6356e-012  4.1189e-011
  6.1957e-010 -7.2226e-009
 -5.7064e-008  6.8914e-007
  3.0750e-006 -3.8804e-005
 -9.8162e-005  1.3070e-003
  1.7996e-003 -2.5461e-002

 -1.7782e-002  2.6351e-001
  8.7924e-002 -1.2001e+000
 -6.2491e-002  3.3190e+000
```

In the model a quarter of the mean and variance echo power distribution in polar coordinates is calculated from these coefficients by:

```
for
r = 1:length(RadiusVec)
p = diag(AMeanPower(:,:,k)*repmat([RadiusVec(r).^[9:-
1:0]],11,1)');
y = polyval(p(1:10),AzimuthVec,9);
Pm(:,r) = y';              % Quarter of power distribution mean
p = diag(AMeanPowerSigma(:,:,k)*repmat([RadiusVec(r).^[9:-
1:0]],11,1)');
y = polyval(p(1:10),AzimuthVec,9);
Ps(:,r) = y';              % Quarter of power distribution sigma
End
```

where *k* is the index of the elevation and:

```
RadiusVec = [0:2:250];    % Model radius grid in m
AzimuthVec = [0:2:90];    % Model azimuth grid in degrees
```

6 User motion

This channel model is designed to provide the user with a time variant speed, time variant heading and satellite elevation. In simulations, the selection of the user motion has a significant influence on the performance of the device under test (DUT).

For example, in a simulation using a slow motion user profile, echoes exist over long time intervals. A navigation receiver that estimates the channel impulse response and is designed to use the coherence length of the channel for improved accuracy can benefit from the long coherence length. A standard DLL receiver will result in large errors. If a high speed motion profile is used, the echoes become extremely short and the estimation receiver can no longer estimate the channel

properly which will result in larger errors where a standard DLL will average over a certain time period and eliminate most of the error. This example shows that this influence can be very large and can even change the performance order of satellite receivers. Therefore, the user motion profile has to be selected with care. Two distinct cases are described in the subsections below.

The user motion indicated in this section does not incorporate antenna patterns and variations due to antenna gain due to user dynamics (for example, a pedestrian user with a mobile terminal tends to change randomly the direction of the antenna boresight).

6.1 Case 1: Specific case simulation

In this case, the intention is to simulate the performance of a specific receiver on a specific route through a specific city (real or hypothetical) with a given set of values (e.g. measured speed, azimuth and satellite elevation). The result of this simulation will be accurate but only valid for this case. This is useful if the simulation is, for example, iterated in different runs over a range of azimuths (e.g. 0, 10, 20, 30 …. 350°). Then the result of the simulations can be compared for the different azimuths and will show which azimuth is the best and which is the worst case.

Another example is the iteration of the user speed for a given track: in this case the speed of the different simulation runs is varied (e.g. 10 km/h, 20 km/h …. 80 km/h). The result of the simulation runs will show the influence of the speed to the navigation error.

In addition, the model can be fed with measured speed, heading and elevation data. In this case, the simulation will give the exact result for a user driving on this road. An extrapolation to other tracks is not possible.

For all applications where a user motion profile can be generated *a priori* it is suggested to use such a generated profile.

6.2 Case 2: Statistical simulations (Monte Carlo simulation)

Often the goal is not to vary the user movements but parameters that are not motion dependent such as receivers, satellite signals, satellite power, etc. In these cases, it is advisable to reduce the dependence on geometric parameters as much as possible.

To simulate the dependence of the system on a single parameter, it is necessary to reduce the dependence of the simulation on all other parameters as much as possible. Therefore, it is advisable to use the following a set of parameters which will allow for comparing results from different research organizations:

FIGURE 79

Full circle track illustrated

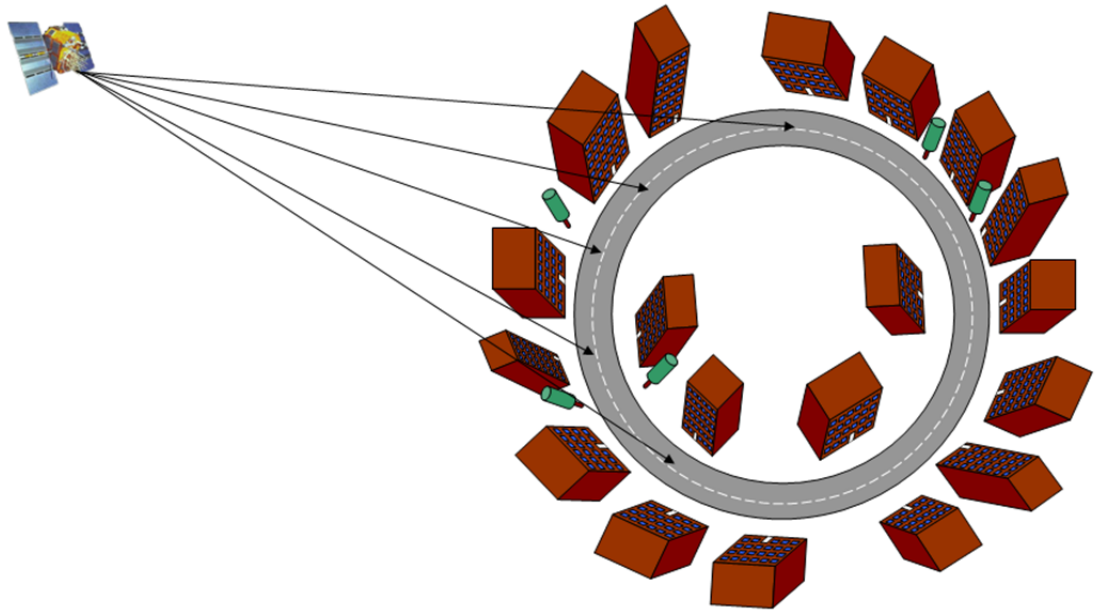

6.2.1 Car Profile – Car A

For convenience this profile is called "ITU P.2145 – Car A"

a) User direction and satellite azimuth

The simulation result strongly depends on the relative angle between the direction of the vehicle and the satellite azimuth. For example, if the satellite is located at a relative azimuth along the direction of movement, the channel will be in line-of-sight conditions most of the time. However, if the satellite is located in a relative azimuth perpendicular to the direction of movement, the signal is often shadowed (especially for low elevations). Therefore a selection of a route where the satellite is more often in the front would result in a higher accuracy than if the satellite is at the side. If the heading is chosen randomly during a simulation (e.g. by a random walk) this can happen accidentally between two simulation runs and may give misleading results.

Therefore, it is suggested to use a large circular road so that it covers all user directions evenly. A period of 1800 s to cover a 360° change in direction is an adequate choice. For longer simulation times, a multiple of full circles ($N = 1,2,3$ ...) shall be considered. This results in a simulation time of $N \times 1800$ s.

b) Satellite elevation

It is suggested to keep the elevation of the satellite constant over the full circle to avoid a mixed dependence on elevation and azimuth.

c) User speed

A time cycle of 60 s over which the user speed changes is suggested, including high-speed movements, stop phases and low speed movements. This profile simulates a stop and go situation in urban traffic. This profile is shown in Fig. 80.

FIGURE 80

Speed profile for car applications – Profile "ITU P.2145 – Car A"

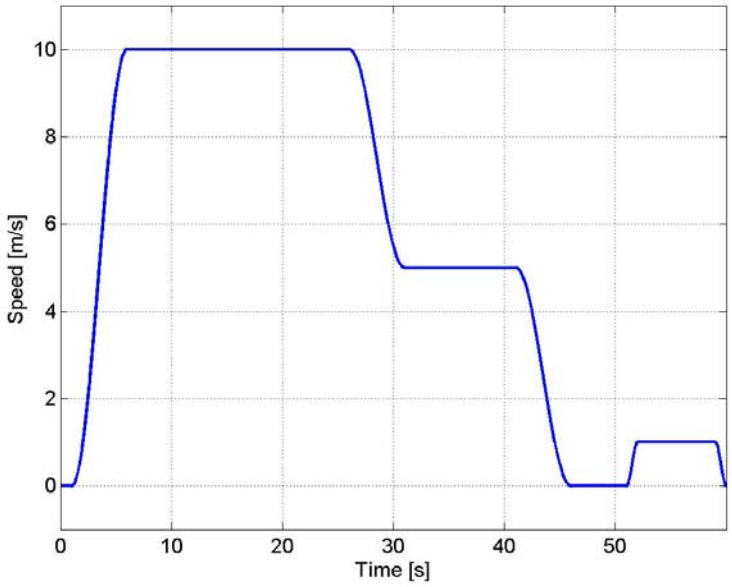

d) Receiver height

For the car application, it is suggested to use a constant antenna height of 1.5 m.

6.2.2 Pedestrian profile – "Pedestrian A"

For this application, a profile that represents a stop and walk cycle is suggested. In contrast to a car application, it is assumed that the user walks only at one speed.

For convenience this profile is called "ITU P.2145 – Pedestrian A"

e) User direction and satellite azimuth

As in the case of the car profile "Car A", the simulation result strongly depends on the relative angle between the direction of the pedestrian and the satellite relative azimuth. Once again, a large circular road is advised.

f) Satellite elevation

To avoid a mixed dependence on elevation and azimuth, it is suggested to keep the elevation of the satellite constant over the full circle.

g) User speed

A time cycle of 60 s over which the user speed changes is suggested. This profile is presented in Fig. 81.

FIGURE 81

Speed profile for pedestrian applications – Profile "ITU P.2145 – Pedestrian A"

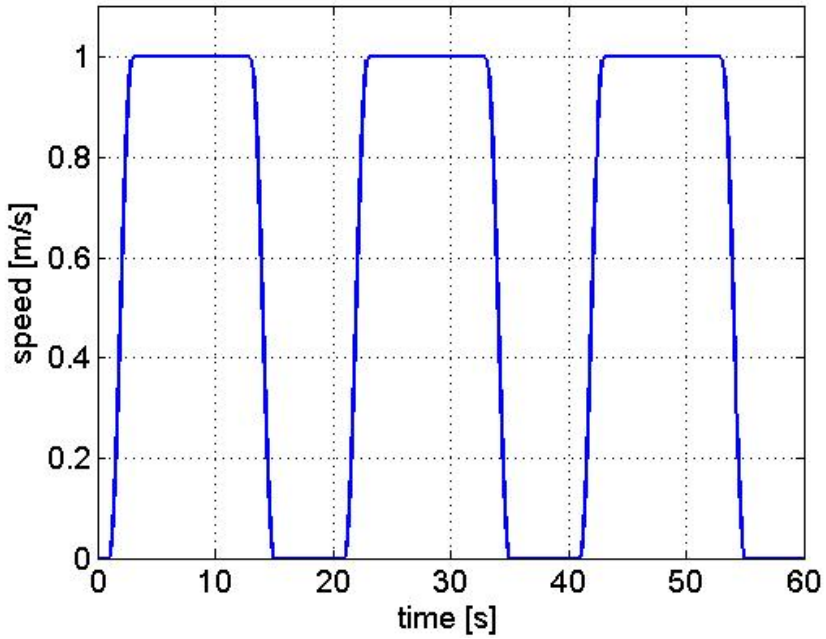

h) Receiver height

In a pedestrian application, the device is often a handheld. While walking, this height can vary due to the movement of the user's hand. To simulate a time variant antenna height a profile like the one presented in Fig. 82 is advised.

FIGURE 82

Antenna height for pedestrian applications – Profile "ITU P.2145 – Pedestrian A"

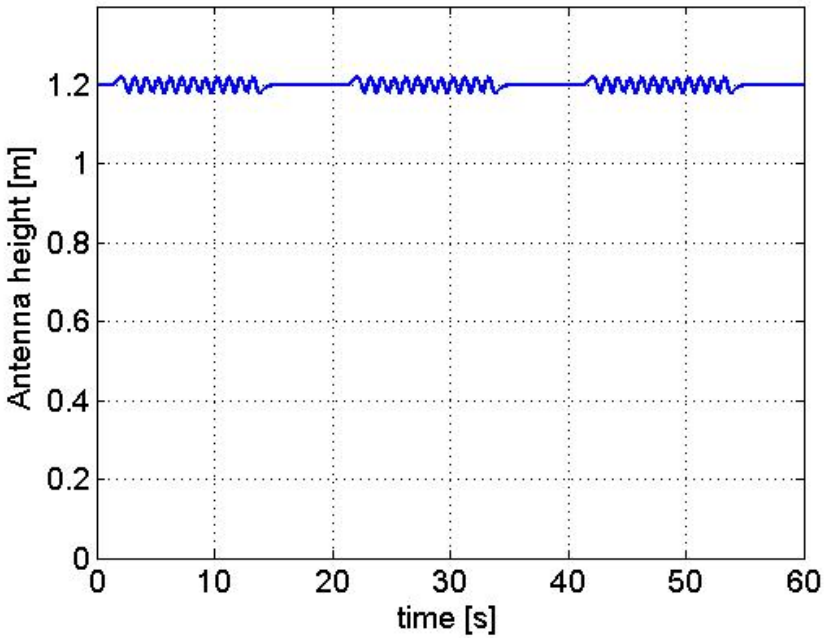

7 Acronyms

CDF	Cumulative distribution function
CIR	Channel impulse response
FIR	Finite impulse response
IDFT	Inverse discrete Fourier transform
LMSCM	Land mobile satellite channel model
LoS	Line of sight

8 IPR protection

Some methods of this channel model are protected by filed or granted patents. The German Aerospace Center has signed the patent statement and licensing form of the ITU to allow unlimited and non-discriminatory access to licenses concerning these patents.

References

KAMMEYER, K.D. and KROSCHEL, K. [2002] *Digitale Signalverarbeitung*. B. G. Teubner Verlag.

LEHNER, A. [2007], Multipath Channel Modelling for Satellite Navigation Systems PhD Thesis, University of Erlangen-Nuremberg, ISBN 978-3-8322-6651-6, Shaker Verlag GmbH, D-52018 Aachen, Germany.

SKLAR, B. [1998] *Digital Communications.* Prentice Hall.